

Control of domain states in rhombohedral PZT films via misfit strains and surface charges

Ivan S. Vorotiahin^{* a,b}, Anna N. Morozovska^b, Eugene A. Eliseev^c, Yuri A. Genenko^a

^a Technical University of Darmstadt, Institute of Materials Science, Otto-Berndt-Str. 3, 64287 Darmstadt, Germany

^b Institute of Physics NAS of Ukraine, Prospekt Nauky 46, 03028 Kyiv, Ukraine

^c Institute for Problems of Materials Science NAS of Ukraine, Krzhizhanovskoho str. 3, 03142 Kyiv, Ukraine

Abstract

Using the Landau-Ginzburg-Devonshire theory, an influence of the misfit strain and surface screening charges, as well as the role of the flexoelectric effect, has been studied by numerical modelling in the case of a rhombohedral lead zirconate-titanate ferroelectric/ferroelastic thin film with an anisotropic mismatch produced by a substrate. It was established that the magnitude and sign of the misfit strain influence the domain structure and predominant directions of the polarization vector, providing misfit-dependent phases with different favourable polarization components. Whilst strong enough compressive misfit strains favour a phase with an orthorhombic-like polarization directions, strong tensile misfits only yield in-plane polarization components. The strength of surface screening is seen to condition the existence of closure domain structures and, by increasing, supports the single-domain state depending on the value of the misfit strain. A crucial role of the flexoelectric effect is revealed as it saves the polar state of the film at high tensile misfit strains. Without the flexoelectric effect, the growing tensile misfit strain eventually suppresses the polarization, and hence any domain structure. Cooperative influence of the misfit strain, surface screening charges and temperature can set a thin rhombohedral ferroelectric film into a number of different polar and structural states, whereby the role of the flexoelectric effect is significant for establishing its phase diagram.

Keywords: Ferroelectrics, Strain Engineering, Flexoelectricity, Rhombohedral

1. Introduction

Thin films of lead zirconate-titanate (PZT) belong to the most widely used ferroelectric materials, having excellent piezoelectric properties and phase diagrams that allow using their whole potential in electronic devices [1, 2, 3, 4, 5, 6, 7]. Their properties are mostly well-known and thoroughly analysed [8, 9, 10, 11, 12, 13, 14]. In comparison with other phase symmetries, rhombohedral thin films of PZT are known to exhibit extra high piezoelectric properties [15]. However, understanding of their important features is still lacking, particularly, of the role of the flexoelectric effect, which is especially pronounced in thin films.

* Corresponding author, e-mail: isvort@mm.tu-darmstadt.de

To control the ferroelectric polar states of thin films the influence of the substrate-induced mismatch strain, flexoelectricity, and surface screening charges on the phase formation should be considered in conjunction with each other. This can be done by analysing strain-dependent phase diagrams obtained from numerical and analytical calculations within the framework of the Landau-Ginzburg-Devonshire theory [16, 17].

The influence of the misfit strain caused by the substrate on the properties of the film is a cornerstone of strain engineering [18]. It can increase or suppress polarization [19], favour one structural phase over another [20], and stabilize certain domain structures [21].

Flexoelectric effect, though being weak, gains greater impact, when dealing with thin films, and can be critically important for some physical properties [22, 23]. An inherent property of virtually all solid materials, this electromechanical effect binds strain gradients and polarization in case of the direct flexoelectric effect and polarization gradient with elastic strain or stress in the conversed effect case. The most natural regions for the flexoelectricity to manifest itself in ferroelectric and ferroelastic structures are domain walls [24, 25], structural defects [26], and strained (e.g. due to the substrate mismatch) surfaces creating strain gradients across the films [27, 28, 29]. Ferroelectric thin films are suitable for detecting flexoelectricity for several reasons. They have high dielectric permittivity and molecular structures with mobile ions, displacement of which is responsible for spontaneous polarization occurrence, which also enhances the flexoelectric effect. The small-size scales of thin films also facilitate the detection of flexoelectricity, as it influences macroscopic properties stronger. Flexoelectricity affects such properties as dielectric permittivity [30, 31], critical thickness of ferroelectricity [32] and domain-wall conductivity [33, 34]. It shifts ferroelectric hysteresis loops by voltage, creating a so-called built-in potential [35, 36, 37, 38] (or even switches polarization actively [39, 40, 41]), generates morphotropic phase boundary (MPB)-like rotations of the spontaneous polarization [42], and invokes other effects like polarization induced bending [43], modification of phonon dispersion curves [44], *etc.* When such films are grown on rigid substrates with a mismatch, the misfit strains may be relieved via formation of local misfit dislocations, which, being inhomogeneous, also promote flexoelectricity [45]. This all means that accounting the flexoelectric effect when studying thin ferroelectric films becomes crucial.

Experimental studies and theoretical modelling of the misfit strain effects have their goal in establishing how the chemical composition and structural properties of specific substrates influence properties of the ferroelectric films being grown on them [46, 47]. Choosing specific combinations of a substrate and a film defines the value and direction of the misfit strain which in turn forms a specific structural phase [48], domain patterns [49, 50, 51], the order of phase transition, or can stabilize polymorphic ferroelectric phases with a coexistence of several structural phases in a way similar to the MPB [52, 53, 54, 55, 56]. In some cases, selected misfit strains help stabilize ferroelectricity in the otherwise paraelectric materials [57, 58, 59, 60, 61]. This is where both well-known [62] and novel [63] materials have a great potential. Generally, domain structures of the epitaxial thin films can be conveniently tailored by misfit engineering and could even be used to develop new types of devices with a domain wall as a functional element [46, 64, 65, 66, 67, 68, 69, 70].

Thin ferroelectric films of various materials, from PZT to BiFeO_3 (BFO) were previously modelled in different structural phases with the Landau-Ginzburg approach [71]. A phase-field study in 2005 [19] has shown that domain morphologies in tetragonal, rhombohedral and orthorhombic PZT films depend on the sign (tensile or compressive) of misfit. Thereby

rhombohedral domain period changes due to a small misfit of $\pm 0.5\%$, while tetragonal structures reconfigure with different polarization components depending on the strength of the tensile misfit. A similar research was conducted later for rhombohedral BFO films [72], where the sign and value of strain applied by the substrate, as well as the orientation of the film on the substrate, determine shapes, sizes and the very existence of domains in a thin film. A step further was a simulation of lead titanate (PTO) nanoparticles of different shapes and the impact of their geometry on phase transition parameters (e.g. Curie temperature) with occurrence of vortex domains [73]. Phase transitions conditioned by epitaxial strain were found and studied by density-functional theory [74]. Employing strains in the range of $\pm 1.5\%$, phase behaviours of barium titanate (BTO) and PTO have been compared and the path of changes between several structural phases with different dominating polarization components was drawn. For BTO, the compressive strain inhibits and even suppresses the transition to the nonpolar phase [75]. The aforementioned appearance of the ferroelectricity in SrTiO_3 under misfit strains was also predicted [76] and investigated phenomenologically [77]. The mentioned modelling studies reveal a great deal about the effect of the mismatch strains. They, however, did not account for the flexoelectric effect, the influence of which becomes significant on those scales. The general framework for the modelling studies consisted of efforts to develop multiscale simulation strategies that connect different theoretical and modelling approaches across a wide range of scales in order to realize a concept of “ferroelectric oxides by design” [46]. Most of the studies, be it theoretical or experimental, focus themselves on the (001)-oriented ferroelectric films due to ease of growth and commercial accessibility of the (001)-cuts [46].

Surface screening charges are responsible for a variety of effects in ferroelectrics. Induced by surface defect states or an electrode, they affect the depolarizing field that influences a domain structure in the film. When the screening is close to the ideal one, it will support a single-domain state or at least would oppose any sort of closure domain structures [78, 79, 80, 81, 82, 83]. Even the non-ideal screening affects polar properties of a ferroelectric film, typically having an impact on the nucleation process, domain shapes and sizes, polarization rotation, broadening of domain walls *etc.* [84, 85, 86, 87, 88, 89, 90, 91, 92, 93, 94, 95, 96]. It is important to keep the surface screening in view or take in into account when studying properties of ferroelectric thin films. Moreover, the surface screening can be controlled which allows tuning film’s properties [97].

The subject of this study is a single-crystalline film of PZT 60/40, which serves as a model material to investigate properties of rhombohedral ferroelectrics on the nanoscale using the phenomenological concept and calculations. The study is performed by means of the time-dependent Landau-Ginzburg-Devonshire theory with a system of equations incorporating important electrostatic and mechanical interactions, including electrostriction and the flexoelectric effect. The model and its constitutive equations are presented in Section 2. Section 3 displays the modelling results from two main perspectives: the spatial distributions of electrostatic and mechanical quantities and their characteristics (Section 3.1), and a quantitative analysis of the structural parameters and the phase stability of the system (Sections 3.2 and 3.3). The influence of the surface screening is studied in Section 3.4. It is followed by a general discussion in Section 4.

2. Theory and Methods

2.1. Problem Layout

Considered is a thin ferroelectric film of thickness h , attached to a bottom metallic electrode and exposed to the ambience from the top side. Up above, in the ambience, on a distance h_v from the top surface, there is a top metallic electrode. Both electrodes are kept at fixed potentials. The thin film consists of PZT 60/40, which at room temperature has a rhombohedral crystalline structure. In absence of any misfit strains between the substrate and the film, a domain structure spontaneously forms with time.

Material parameters for the PZT 60/40 used here can be found in **Appendix A**.

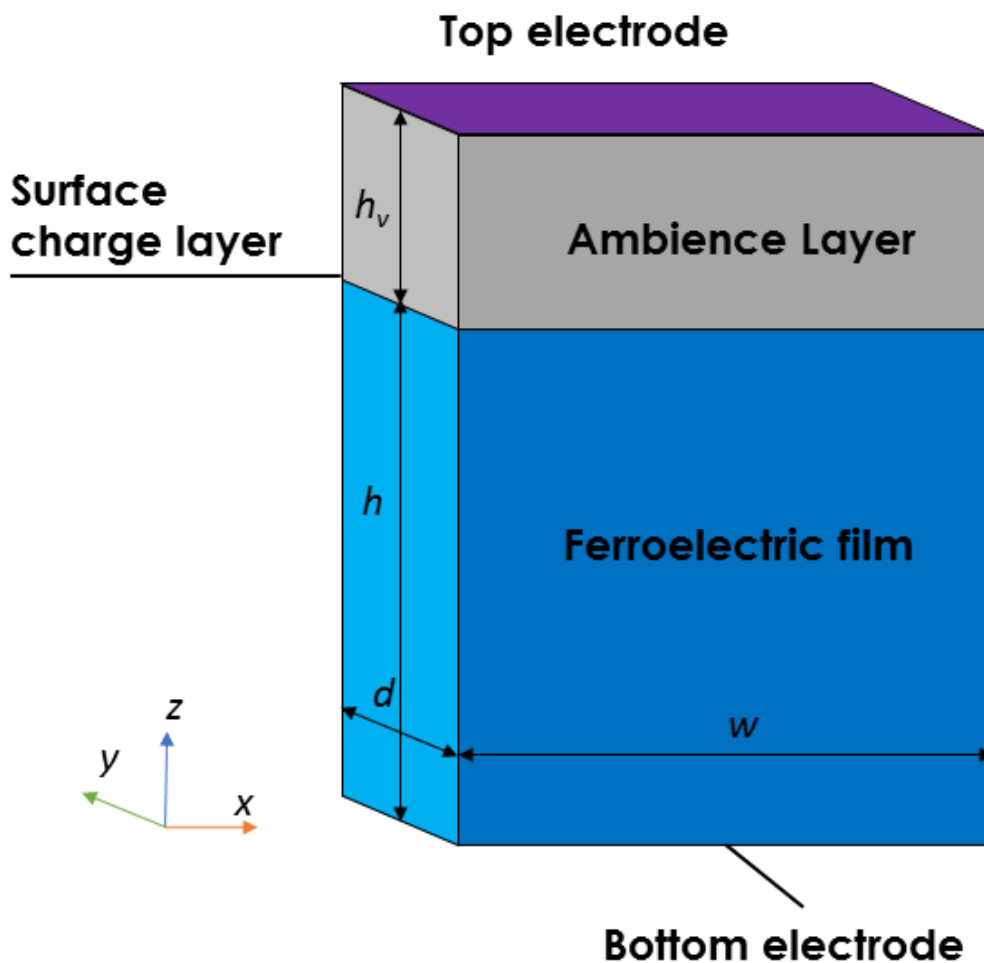


FIGURE 1. Problem layout. A ferroelectric film of thickness h , width w and depth d on the bottom electrode with an ambience layer of thickness h_v on the top. A layer of screening charge on the top surface of the film separates it from the ambience. Here and afterwards, a correspondence shall be assumed between $x = x_1$, $y = x_2$, and $z = x_3$.

2.2. Gibbs Free Energy Functional

The Gibbs thermodynamic potential of the whole system can be described as a sum of a volume free energy, a surface free energy, and an ambience free energy:

$$G = G_V + G_S + G_A . \quad (1)$$

In relation to polarization \mathbf{P} , electrostatic potential φ and elastic stress σ , the volume, surface and ambient parts of the Gibbs free energy respectively read as following:

$$G_V = \int_V d^3r \left(\frac{\alpha_{ik}}{2} P_i P_k + \frac{\beta_{ijkl}}{4} P_i P_j P_k P_l + \frac{\gamma_{ijklmn}}{6} P_i P_j P_k P_l P_m P_n + \frac{g_{ijkl}}{2} \left(\frac{\partial P_i}{\partial x_j} \frac{\partial P_k}{\partial x_l} \right) \right. \\ \left. - P_i E_i - Q_{ijkl} \sigma_{ij} P_k P_l - \frac{s_{ijkl}}{2} \sigma_{ij} \sigma_{kl} - F_{ijkl} \sigma_{ij} \frac{\partial P_l}{\partial x_k} \right), \quad (2a)$$

$$G_S = \int_S \left(\frac{\alpha_{ij}^S}{2} P_i P_j - \frac{\varepsilon_0}{2\lambda} \varphi^2 \right) d^2r, \quad (2b)$$

$$G_A = - \int_A \frac{\varepsilon_0 \varepsilon_v}{2} E_i E_j d^3r . \quad (2c)$$

As mentioned in Table I, the coefficients of the Landau expansion by the powers of polarization are α_{ik} , β_{ijkl} and γ_{ijklmn} ; g_{ijkl} is the gradient coefficient tensor. E_i is the electric field component; σ_{ij} is the elastic stress tensor, Q_{ijkl} is the electrostriction tensor, F_{ijkl} is the flexoelectric effect tensor, s_{ijkl} is the elastic compliance. α_{ij}^S is a surface stiffness tensor, here and after presumed to be zero, λ is the surface screening length parameter for the Bardeen model of surface charges. ε_0 is the dielectric constant for the vacuum, and ε_v is a relative dielectric constant of the ambience.

2.3. System of Equations

Equations solved in this study include the Landau-Khalatnikov equations for three polarization components P_i , the Poisson equation for the electrostatic potential φ , and the equilibrium condition for elastic stress components σ_{ij} .

Landau-Khalatnikov Equation

The time-dependent Landau-Ginzburg-Devonshire equation can be obtained from the variation of the Gibbs free energy with respect to the order parameter of polarization,

$$\Gamma \frac{\partial P_i}{\partial t} = - \frac{\delta G_V}{\delta P_i} . \quad (3)$$

The equation reads explicitly as follows:

$$\Gamma \frac{\partial P_k}{\partial t} + \alpha_{ik} P_i + \beta_{ijkl} P_i P_j P_l + \gamma_{ijklmn} P_i P_j P_k P_l P_m P_n - g_{ijkl} \left(\frac{\partial^2 P_i}{\partial x_j \partial x_l} \right) - 2Q_{ijkl} \sigma_{ij} P_l + F_{ijkl} \frac{\partial \sigma_{ij}}{\partial x_l} = - \frac{\partial \varphi}{\partial x_k} . \quad (4)$$

Boundary conditions for top and bottom surfaces includes flexoelectric coupling

$$\left. \left(g_{ijkl} \frac{\partial P_i}{\partial x_j} - F_{ijkl} \sigma_{ij} \right) \right|_{x_3=0,h} = 0 . \quad (5)$$

Poisson Equation

The electrostatic properties of the material can be described using the Poisson equation for the electric potential φ related to the electric field, $E_i = -\nabla_i \varphi$. It contains terms correspondent to the contributions from the crystal lattice itself and ferroelectric polarization. The spatial distribution of φ can be devised both for the film bulk and for the ambience, where the ferroelectric contribution is absent. Thus, for the film the Poisson equation reads as

$$\varepsilon_0 \varepsilon_b \frac{\partial^2 \varphi}{\partial x_i \partial x_i} = \frac{\partial P_j}{\partial x_j} , \quad (6a)$$

while in the ambience it turns into the Laplace equation,

$$\varepsilon_0 \varepsilon_v \frac{\partial^2 \varphi}{\partial x_i \partial x_i} = 0 \quad (6b)$$

with boundary conditions setting up the properties of the bottom electrode (ground), the interface between the film and the ambience, and the top electrode:

$$\varphi|_{x_3=0} = 0 , \left. \left(D_n^{ext} - D_n^{int} + \varepsilon_0 \frac{\varphi}{\lambda} \right) \right|_{x_3=h} = 0 , \varphi|_{x_3=h-0} = \varphi|_{x_3=h+0} , \varphi|_{x_3=h+d} = 0 , \quad (7)$$

where the electric displacement is defined by $\mathbf{D} = \varepsilon_0 \varepsilon_b \mathbf{E} + \mathbf{P}$, and λ is an effective screening length [98, 99].

Generalized Hooke's Law

Mechanical and electromechanical properties of the film are taken into account via the generalized Hooke law that describes relationship between strain and stress within the ferroelectric film with the effects of interest being included, such as electrostriction and flexoeffect. It can be derived by variation of the Gibbs free energy (2a) with respect to stress variable σ ,

$$u_{ij} = s_{ijkl} \sigma_{kl} + F_{ijkl} \frac{\partial P_k}{\partial x_l} + Q_{ijkl} P_k P_l . \quad (8)$$

In the system of equations, elastic variables are governed by an equilibrium condition, namely:

$$\frac{\partial \sigma_{ij}}{\partial x_i} = 0 \quad (9)$$

It is solved with the following (mixed) boundary conditions on mechanical strain u_{ij} and mechanical stress σ_{ij} :

$$u_{11}|_{x_3=0} = u_m , u_{22}|_{x_3=0} = 0 , u_{33}|_{x_3=0} = 0 ; \sigma_{11}|_{x_3=h} = 0 , \sigma_{22}|_{x_3=h} = 0 , \sigma_{33}|_{x_3=h} = 0 , \quad (10)$$

where u_m is the misfit strain.

The system of equations described above has been solved with the finite element method using COMSOL Multiphysics software package. To observe the formation of the domain structure in a small part of the ferroelectric film we have enclosed the region inside the computational box with dimensions of $w \times d \times (h + h_v)$ along, respectively, x_1 , x_2 and x_3 (or, respectively, x , y and z) axes. Periodic boundary conditions were imposed to the boundaries along x_1 and x_2 axes. The dimensions w, d, h , of the computational box are: $w = 24$ nm, $d = (8 - 24)$ nm, $h = 24$ nm.

3. Results

3.1. Domain structures

A series of distributions has been obtained as a result of 3D FEM simulations using COMSOL Multiphysics software. Among those, of interest were the polarization distributions, which illustrate the domain structure that should naturally occur in PZT 60/40 films, as well as mechanical displacement distributions that show a deformation pattern of the film under given conditions.

To establish a role of the substrate, a series of computations has been performed, where the misfit strain on the bottom surface of the film was varied between -2% and 2% with a step of 0.5%. In between the characteristic values of 1% and 1.5%, this step was reduced to 0.1%. The resulting structures vary significantly in directions of their polarization vectors, domain walls, as well as in deformations of films. To compare the domain structures and deformation patterns under different misfits, the directions and length of polarization vectors (Fig. 2) are analysed, as well as the x_1 and x_2 -components of the elastic deformation (Fig. 3). In the Fig. 2, those distributions are represented as vector fields, where a vector direction shows the direction of polarization at a given point, and a vector length represents a relative amplitude of polarization. Average absolute polarization amplitude in the volume, as well as the angle between polarization vectors forming two largest domains in the film are shown in Fig. 4 for a range of misfit strain values. Fig. 5 shows absolute lengths of each polarization vector component averaged over the film volume.

The structure without misfit strains has two main domains, with a closure structure near the top surface. The film's polarization vectors have all three components (Fig. 5), and the film exhibits deformations in all three directions (Figs. 2a, 3). Increasing *compressive* misfit strain in x -direction, the average displacement in x -direction first significantly increases (Fig. 3), and then drops to almost zero (Fig. 3). At the same time, the average displacement in y -direction, being initially strong without misfit, starts dropping, while the angle between the main domains increases, starting from about 71° at zero strain, striving to become 180° (Fig. 4a). At the misfit around -2%, the distortion of the film is strong only in x_2 and x_3 components. In the bulk, where there are no closure domains, the in-plane components of polarization (P_1, P_2) are weakened, the P_1 going extinct, and P_2 decreasing to 0.12-0.15 C/m², leaving the P_3 component of about 0.36 C/m² dominant. No significant dependencies on the presence of flexoeffect were detected

for the negative misfit strains, except for minor changes in domain shapes and precise form of film's deformation.

Without the flexoelectric effect, the system begins to lose its domain structure with increasing of the *tensile* misfit strain. First, the domain walls weaken, and polarization vectors become more aligned in one in-plane direction with only small enclaves of closure domains remaining (Fig. 2c). At a point between +1.4% and +1.5%, polarization disappears, and above that point, the film has no polarization whatsoever. However, if flexoelectricity is accounted for, the polarization survives forming a domain structure that tends to the 180° domain wall with polarization vectors looking predominantly in x_1 -direction in the bulk (Fig. 2d). The film distortion is weak in all directions (Fig. 3).

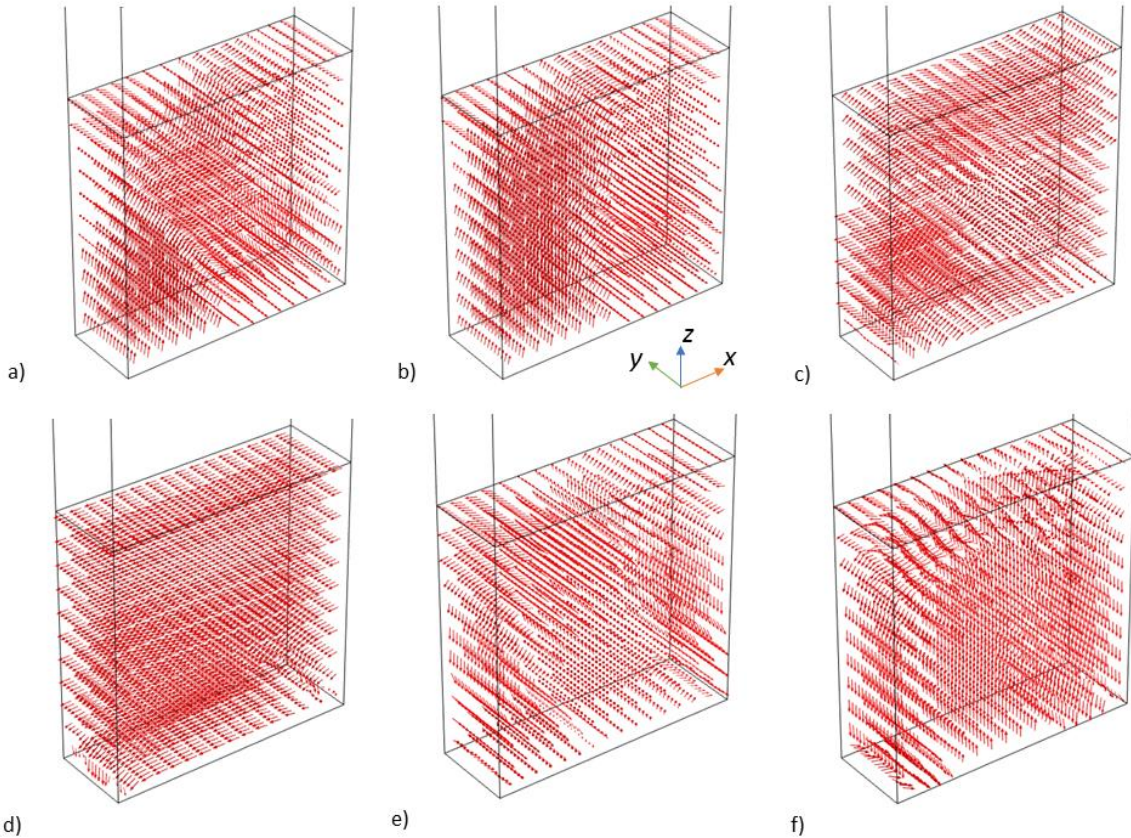


FIGURE 2. Arrow fields of the polarization vector inside a ferroelectric PZT film with (a) flexoeffect and zero misfit strain, (b) zero misfit strain and no flexoeffect, (c) tensile misfit strain 1% and no flexoeffect, (d) misfit strain 2% and flexoeffect, (e) misfit strain -0.5% and flexoeffect, (f) misfit strain -2% and flexoeffect. The computational box has dimensions $h=24$ nm, $w=24$ nm, $d=8$ nm.

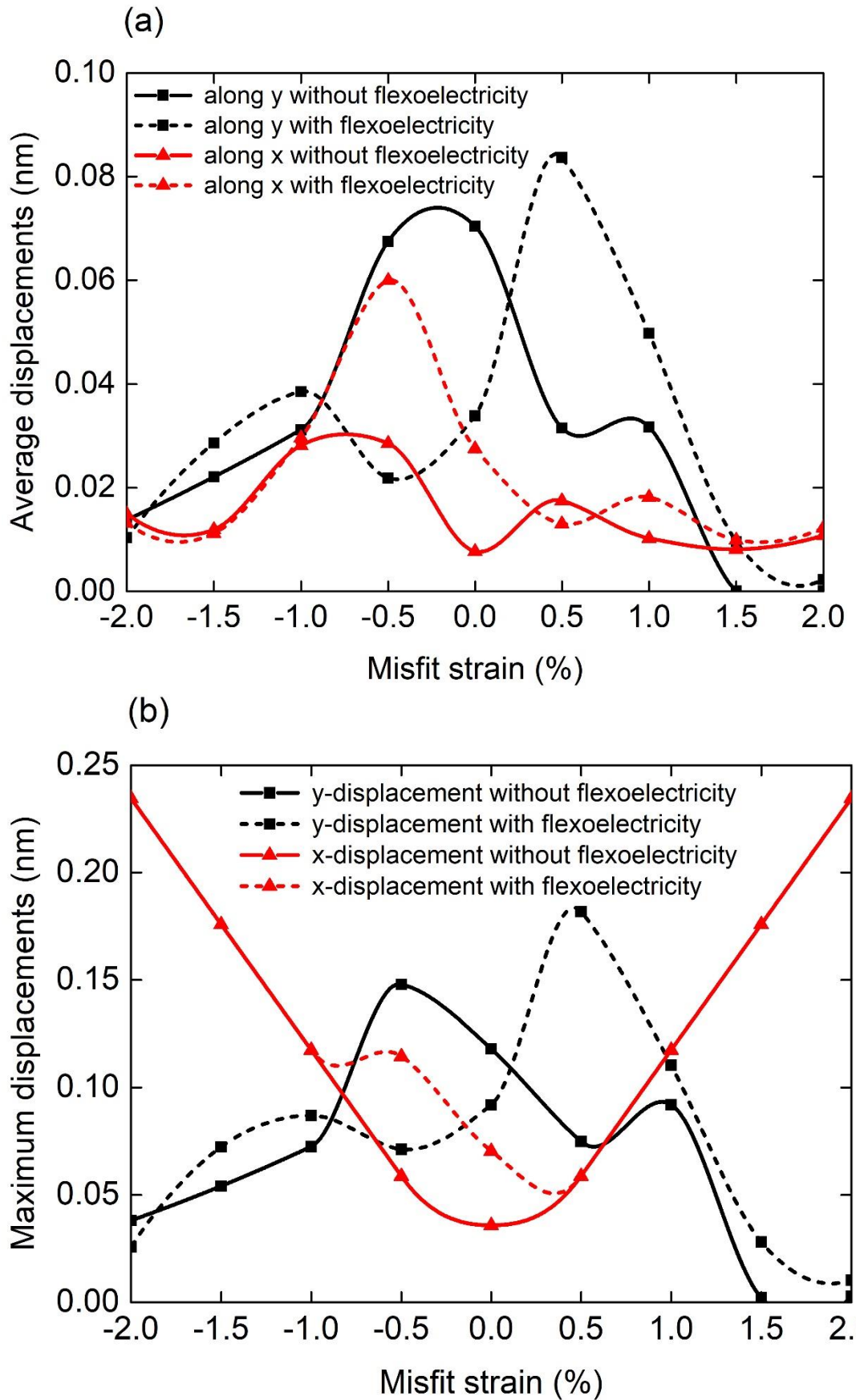


FIGURE 3. Misfit-strain dependencies of (a) the volume average and (b) the volume maximum of the absolute U_1 and U_2 -components of elastic displacement in a thin ferroelectric film.

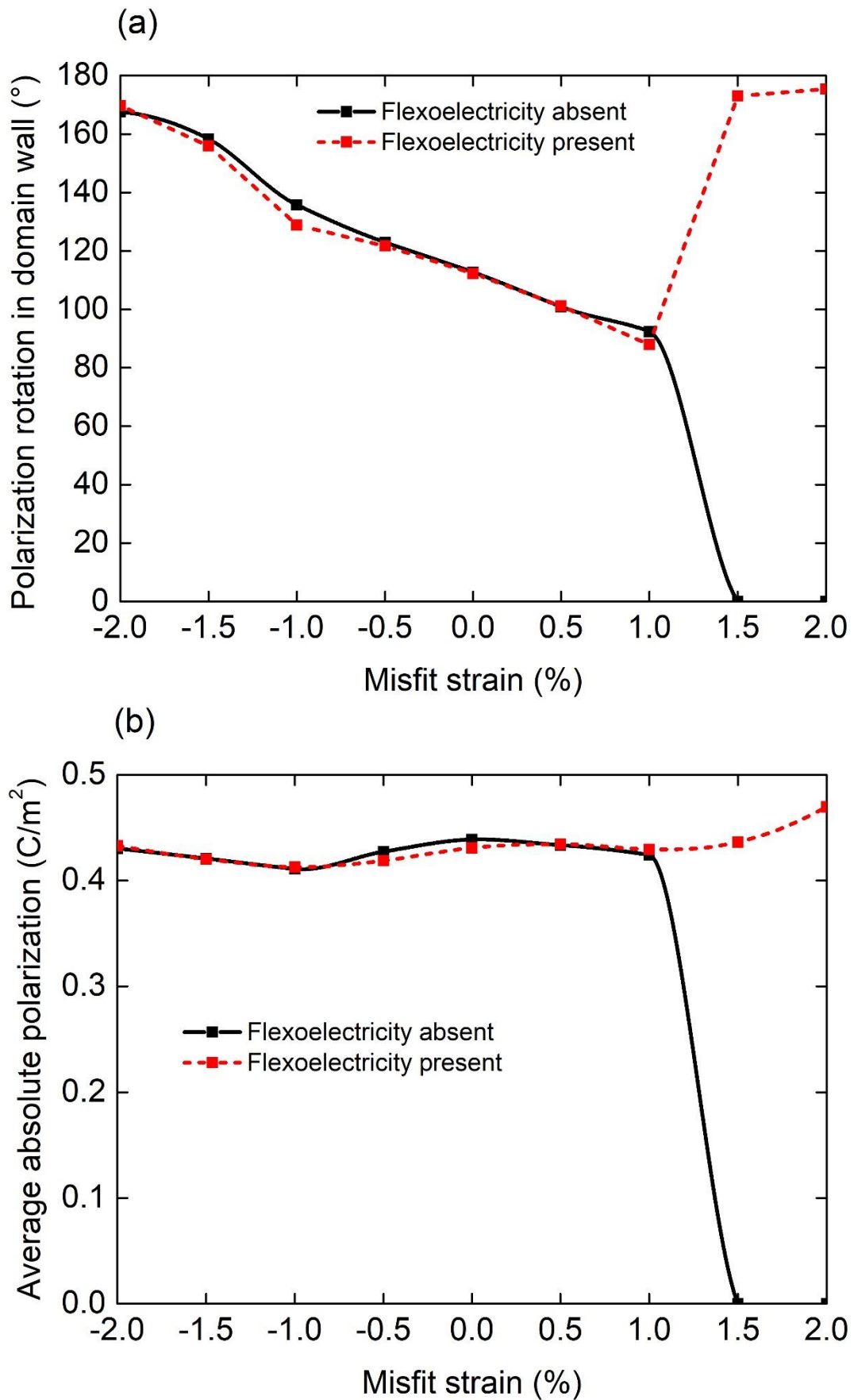


FIGURE 4. Misfit-strain dependencies of (a) the angle between the polarization vectors of the largest domains in a structure and (b) the average length of the polarization vector in a thin ferroelectric film.

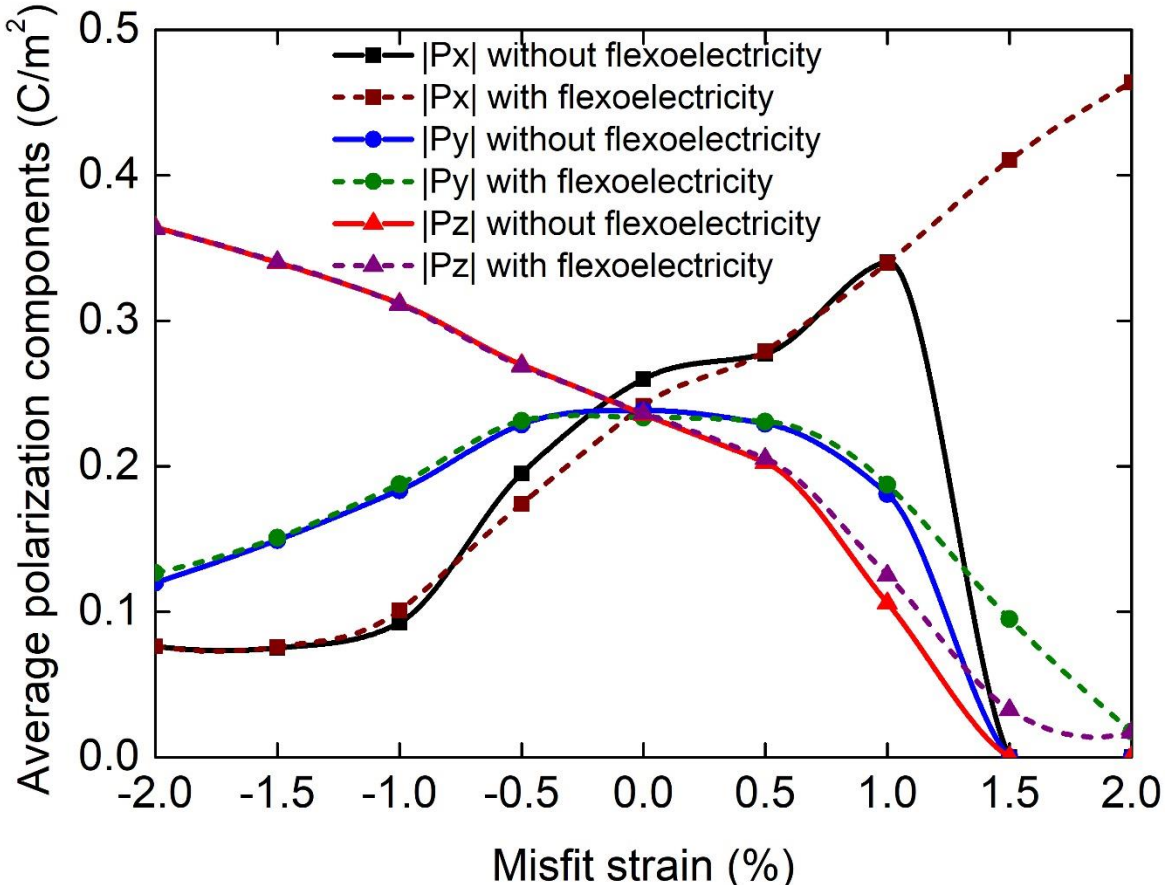


FIGURE 5. Misfit strain dependencies of the volume average of P_1 , P_2 , and P_3 components of polarization.

From the spatial maps of the polarization vector and the polarization dependencies on misfit strain, different effects of compressive and tensile misfit strains on the rhombohedral PZT film are revealed. The *compressive* misfit strain is observed to favour the polarization domain structures and brings about film deformations. Those deformations have all three spatial components when small misfit strain is applied, so that the P_1 polarization component is the strongest when misfit strain is about -0.5% (Fig. 5a). Thereby there are strong displacements by all three spatial components, the way we would expect from a rhombohedral film. Stronger compressive misfit strains, on the contrary, diminish the U_2 deformations, that are perpendicular to the direction x_1 of the applied misfit strain, so that at the misfit of -2%, the film is almost exclusively displaced by only two spatial coordinates, which is the way we would rather expect from the orthorhombic structure. The distortions alone, however, cannot speak of the preferred structure type, and angles between polarization directions in different domains do not allow determining it for sure either. The *tensile* misfit strains show another behaviour, at which the film gradually loses its polarization domain structure coming close to a phase boundary with the paraelectric state at the misfit strain of 1.4%. At higher misfit strains there would be no polarization whatsoever in the absence of flexoelectricity, but the flexoelectric effect supports the polar phase, albeit without a solid domain structure, and with dominant P_1 polarization component, along the direction of the applied misfit strain.

3.2. Flexoelectric Impact on Domain Structure

Displayed in Fig. 2 polarization vector maps allow us to deduce domain structures within the film, and their changes due to the application of misfit strains. The other factor that also affects the form of domains is the presence of the flexoelectric effect. The flexoelectric coupling influence is different in the two opposite regions of the misfit strain range. The influence is critical at greater tensile misfit values; it is the weakest in the absence or at small misfits and rises up again at greater compressive misfit strains. Though not of the critical nature, the flexoelectric impact at compressive misfit strains is still visible quantitatively. To help deduce important parameters quantifying that influence, analytical calculations were conducted.

3.2.1. Impact of the flexoelectric coupling and gradient terms

The impact of the flexoelectricity and gradient effects within the Gibbs free energy density is presented by following terms:

$$g_{LGD} = g_L + g_{grad} + g_{flexo}, \quad g_{grad} = \frac{g_{ijkl}}{2} \frac{\partial P_i}{\partial x_j} \frac{\partial P_k}{\partial x_l}, \quad g_{flexo} = \frac{f_{ijkl}}{2} u_{ij} \frac{\partial P_k}{\partial x_l}, \quad (11)$$

where g_L is given by Eq. (B1), the elastic strains are given by Eq. (8) and full matrix notations are used. The substitution of the electrostrictive part of the strains (a toy model for which the term $s_{ijkl}\sigma_{kl}$ can be regarded small) leads to:

$$\begin{aligned} \delta g_{grad+flexo} &= \frac{g_{ijkl}}{2} \frac{\partial P_i}{\partial x_j} \frac{\partial P_k}{\partial x_l} + \frac{f_{ijkl}}{2} \left(Q_{ijmn} P_m P_n + F_{ijmn} \frac{\partial P_m}{\partial x_n} \right) \frac{\partial P_k}{\partial x_l} \\ &\equiv \left(\frac{g_{ijkl}}{2} + \frac{f_{qskl}}{2} F_{qsi} \right) \frac{\partial P_i}{\partial x_j} \frac{\partial P_k}{\partial x_l} \equiv \frac{1}{2} (g_{ijkl} + s_{qsmn} f_{qskl} f_{mnij}) \frac{\partial P_i}{\partial x_j} \frac{\partial P_k}{\partial x_l} \equiv \frac{1}{2} g'_{ijkl} \frac{\partial P_i}{\partial x_j} \frac{\partial P_k}{\partial x_l}. \end{aligned} \quad (12)$$

Since the term $\frac{f_{ijkl}}{2} Q_{ijmn} P_m P_n \frac{\partial P_k}{\partial x_l}$ has (almost) zero average, it can be omitted, and then the renormalized gradient coefficient $g'_{ijkl} = g_{ijkl} + s_{qsmn} f_{qskl} f_{mnij}$ can be introduced. The renormalization has different signs for the diagonal and non-diagonal components, but for the cases of interest, $g'_{11} = g_{11} + s_{qqmm} f_{qq11} f_{mm11}$ and $g'_{44} = g_{44} + s_{qqmm} f_{qq44} f_{mm44}$, it (typically) increases g_{11} and decreases g_{44} . For a cubic symmetry of the parent phase, the trend $g'_{11} > g_{11}$ and $g'_{44} < g_{44}$ is responsible for the increase of intrinsic width of the charged domain walls/structures/configurations, and decrease of the width of uncharged domain walls. Since the uncharged walls are the most common, being significantly more preferable from the energetic viewpoint [100, 101], the flexoelectricity induces and facilitates their curvature, meandering and labyrinthine configurations in multiaxial ferroelectrics at $g'_{ijkl} < g_{ijkl}^{cr}$ (see e.g. [97, 102, 103]). At the same time, the condition $g'_{44} < g_{44}$ increases, while not very strongly, the transition temperature from the ferroelectric to paraelectric phase (see e.g. [18, 104]). The strong influence of the flexoelectricity comes from the flexo-dependent boundary conditions in strained thin films, $\left(g_{kjm} n_k \frac{\partial P_m}{\partial x_j} + a_{ij}^S P_j - F_{jkm} \sigma_{jk} n_m \right) \Big|_{x_3=h} = 0$ (see e.g. Ref.

[104] for details). The term $F_{jkim}\sigma_{jk}n_m$, proportional to the flexoelectric coupling strength, can lead to the appearance of built-in inhomogeneous flexo-electric fields with specific geometry.

Actually, due to the flexoelectric effect, there is no size-induced transition to a paraelectric phase down to (2 – 4) nm thickness of PbTiO_3 [001]-oriented films with 1% of compressive misfit strain [104]. The origin of this phenomenon is the re-building of the domain structure in the film (namely the cross-over from *c*-domain stripes to *a*-type closure domains) emerging with its thickness decrease below 4 nm, and conditioned by the flexoelectric coupling.

3.2.2. Fitting of FEM profiles

To identify domain structures in complicated spatial polarization patterns of Fig. 2, distributions of an out-of-plane polarization component along two in-plane directions were derived from the FEM calculations and approximated using analytical functions in a form of a hyperbolic tangential polynomial.

$$P_3(x_1, x_2 = 0) = P_{a1} \tanh\left(\frac{x_1 + x_{01}}{R_{x1}}\right) + P_{a2} \tanh\left(\frac{x_1 + x_{02}}{R_{x2}}\right) + P_{a3} \tanh\left(\frac{x_1 + x_{03}}{R_{x3}}\right). \quad (13a)$$

$$P_3(x_1 = 0, x_2) = P_{a1} \tanh\left(\frac{x_2 + y_{01}}{R_{y1}}\right) + P_{a2} \tanh\left(\frac{x_2 + y_{02}}{R_{y2}}\right) + P_{a3} \tanh\left(\frac{x_2 + y_{03}}{R_{y3}}\right). \quad (13b)$$

Here, P_{ai} is the characteristic magnitudes of different tangential profiles of polarization, and the values R_{xi} and R_{yi} determine the widths of corresponding domain walls (i.e. there are 3 simple tanh-like walls in Eqs.(13)). Figures 6-7 show the distributions of P_1 and P_2 polarization components, along with their analytical fitting for the misfit strain $u_m = 0$ (Fig. 6) and $u_m = -2\%$ (Fig. 7). For the cases $u_m = 0$ and $u_m = -2\%$ Eqs. (13) were used with the parameters listed in **Tables I** and **II**, respectively.

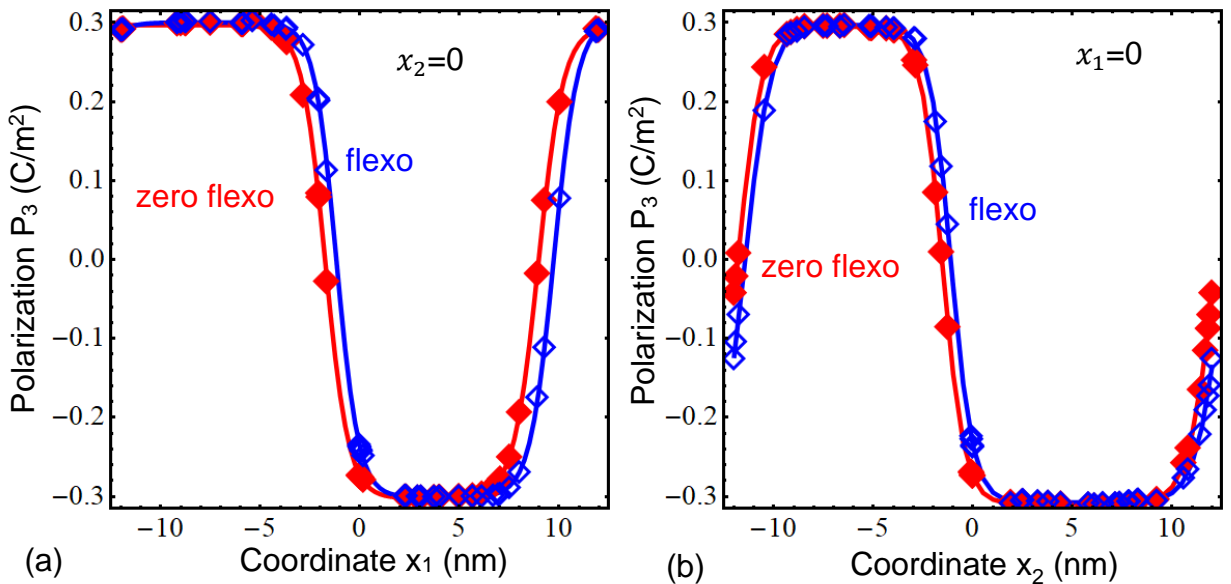


FIGURE 6. Polarization component P_3 profiles in two different cross-sections, **(a)** $x_2=0$ and **(b)** $x_1=0$ calculated for two different models, excluding and including flexoelectric coupling (red and blue symbols+curves, respectively). Diamonds represent the results of FEM calculations, while solid curves are the fitting with Eqs. (13) using parameters summarized in **Tables I**. Misfit strain is zero.

Table Ia. Fitting parameters for the distribution $P_3(x_1)$ for zero misfit strain

parameter	P_{a1} (C/m ²)	R_{x1} (nm)	x_{01} (nm)	P_{a2} (C/m ²)	R_{x2} (nm)	x_{02} (nm)	P_{a3} (C/m ²)	R_{x3} (nm)	x_{03} (nm)
“zero flexo”	0.30	1.487	15.1	-0.30	1.17	1.75	0.30	1.25	-8.96
“nonzero flexo”	0.30	1.335	14.7	-0.30	1.12	1.19	0.30	1.20	-9.73

Table Ib. Fitting parameters for the distribution $P_3(x_2)$ for zero misfit strain

parameter	P_{a1} (C/m ²)	R_{y1} (nm)	y_{01} (nm)	P_{a2} (C/m ²)	R_{y2} (nm)	y_{02} (nm)	P_{a3} (C/m ²)	R_{y3} (nm)	y_{03} (nm)
“zero flexo”	0.28	1.16	11.8	-0.30	1.09	1.5	0.29	1.31	-12.1
“nonzero flexo”	0.30	1.26	11.4	-0.30	1.09	1.1	0.30	1.35	-12.6

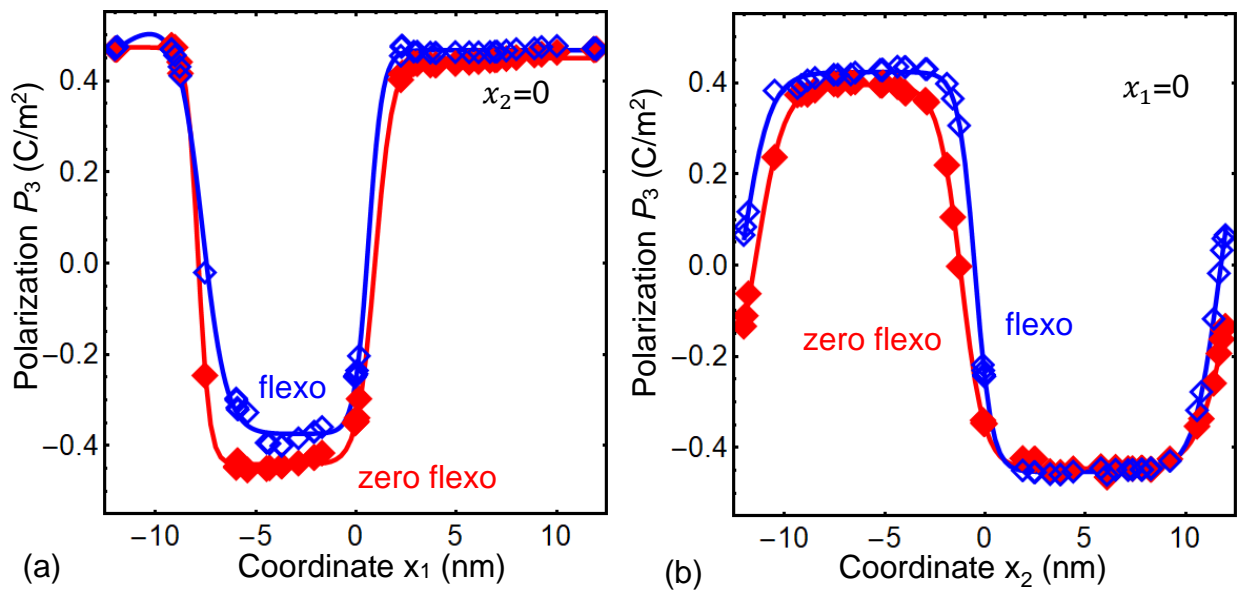


FIGURE 7. Polarization component P_3 profiles in two different cross-sections, **(a)** $x_2=0$ and **(b)** $x_1=0$ calculated for two different models, excluding and including flexoelectric coupling (red and blue symbols+curves, respectively). Diamonds represent the results of FEM

calculations, while solid curves are the fitting with Eqs. (13) using parameters summarized in **Tables II**. Misfit strain is -2 %.

Table IIa. Fitting parameters for the distribution $P_3(x_1)$ for -2% misfit strain

parameter	P_{a1} (C/m ²)	R_{x1} (nm)	x_{01} (nm)	P_{a2} (C/m ²)	R_{x2} (nm)	x_{02} (nm)	P_{a3} (C/m ²)	R_{x3} (nm)	x_{03} (nm)
“zero flexo”	-0.46	0.56	7.88	-0.46	0.07	-18.3	0.45	0.88	-0.95
“nonzero flexo”	-0.43	1.21	7.66	0.51	4.21	16.9	0.42	0.68	-0.62

Table IIb. Fitting parameters for the distribution $P_3(x_2)$ for -2% misfit strain

parameter	P_{a1} (C/m ²)	R_{y1} (nm)	y_{01} (nm)	P_{a2} (C/m ²)	R_{y2} (nm)	y_{02} (nm)	P_{a3} (C/m ²)	R_{y3} (nm)	y_{03} (nm)
“zero flexo”	0.37	1.37	11.4	-0.42	1.14	1.19	0.40	1.63	-12.3
“nonzero flexo”	0.41	1.39	12.2	-0.44	0.82	0.50	0.43	1.29	-11.7

3.3. Phase diagrams of a single-domain state

Obtained polarization distributions indicate domain structures or modulation of polarization oriented in a direction of one or several axes. Parameters of those structures such as the polarization vector length and its components’ absolute values obviously depend on the misfit strain and are expected to depend on the temperature. To quantify these dependences, an analytical solution of the LGD equation system was obtained (see **Appendix B.a.**).

Figure 8 presents an analytically obtained phase diagram for a single domain state of a thin PZT 60/40 film with three polar phases and one nonpolar phase dependent on temperature and uniaxial misfit. The polar phases have the electric polarization oriented in the in-plane (P_1, P_2), out-of-plane (P_3), and mixed directions. The high-temperature phase is nonpolar at small and compressive misfit strains. The out-of-plane polarization (P_3) dominates at the compressive misfit strains and gradually fades with increasing tensile strains. The in-plane component P_1 is, on the contrary, dominant at tensile misfit strains and fades when they become compressive. In case of isotropic biaxial misfit strain (see **Appendix B.b.**), the other in-plane polarization component P_2 reproduces the behaviour of P_1 , and creates an out-of-plane-dominant phase at high compressive misfit strains, an in-plane-dominant phase at high tensile misfit strains, and a mixed (P_1, P_2, P_3) rhombohedral phase between them at small misfit strains.

In the case of anisotropic uniaxial misfit strain, the component P_2 is persistent throughout almost entire misfit range at lower temperatures. It creates a much richer variety of polar phases. The persistent P_2 phase intersects the paraelectric phase, resulting in a small range, where the

P_2 component is dominant. At higher compressive misfit strains P_2 -phase is partially combined with a P_3 -dominant phase, creating a separate phase, where polarization has both P_3 and P_2 components. At higher tensile misfit strains, it creates a band where both P_1 and P_2 can be realized, before the film goes into the P_1 -dominant state. The bottom section of a diagram at lower misfits and lower temperatures represents a phase where all three components of the polarization vector are realized. Dotted lines show how would the phase boundaries change, if it were not a thin film, but a thick ferroelectric bulk.

The single-domain phase diagram can be compared with the FEM results for multi-domain states obtained above, if we draw a line going through the diagram at 300 K. At no misfit and between the values from -1% to +1%, the mixed phase is located with the most thermally stable point at approximately -0.5% strain, where all three components have comparable values (see also Fig. 5). When we proceed increasing the compressive misfit strain, the P_1 value will gradually weaken and vanish at the misfit strain of -1.1%, below which we only see P_2 and P_3 components remaining. When increasing the tensile misfit strain, a similar situation can be observed with fading of the P_3 component, which vanishes at +1% misfit strain. Above this value the polarization vector has only P_1 and P_2 components up until $u_m = 1.9\%$, where P_2 also vanishes, so that the polarization vector is left with only P_1 direction. The analytical phase diagram is, in principle, in agreement with the FEM results, however, Fig. 5 indicates that all components are present, even if with a very weak value, in the whole range of misfit strains. This is due to the existence of closure domains under the free ferroelectric surface that compensate the bound charge created by main domains, which in this case is not screened by an electrode or with surface charge states.

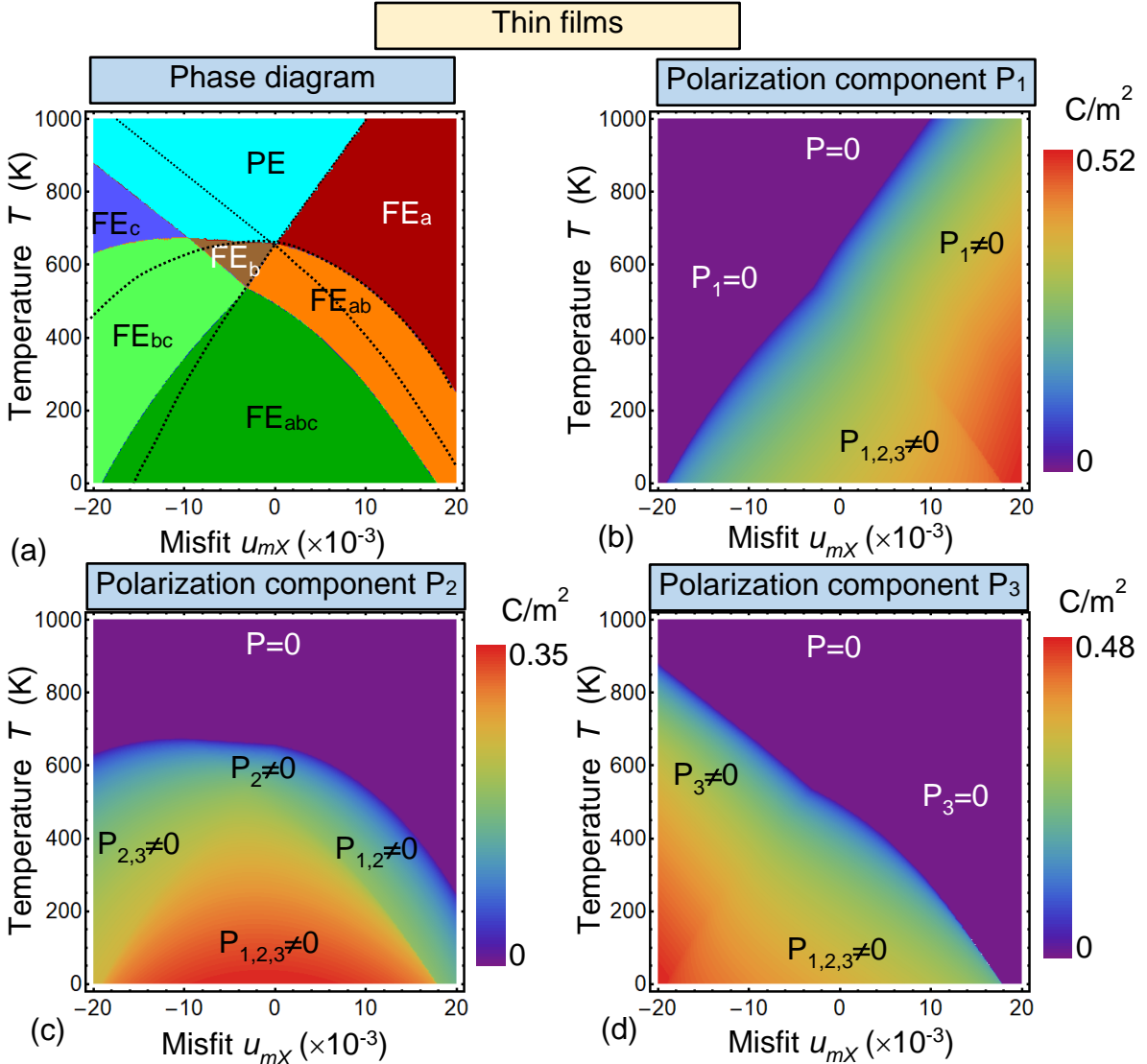


FIGURE 8. (a) Ferroelectric PZT 60/40 phase diagram in coordinates temperature – misfit strain for thin films. Anisotropic uniaxial misfit strain between the film and substrate is considered. Polarization components P_1 (b), P_2 (c) and P_3 (d) dependence on the misfit strain and temperature. Color bars show the range of corresponding values for the contour maps. Paraelectric phase is denoted as “PE”, while “ FE_a ”, “ FE_b ”, “ FE_{ab} ”, “ FE_{abc} ”, “ FE_{bc} ”, and “ FE_c ” show the regions for ferroelectric phases with different orientation of polarization, namely, “a” means P_1 , “b” means P_2 and “c” means P_3 . Film thickness is $h=24$ nm and effective (dielectric) gap width is $d_{eff}=0.12$ nm. Bulk parameters are listed in **Table BI** in **Appendix B**. Here we suppose that $u_{11}^{(m)} \equiv u_{mX}$, while $u_{22}^{(m)} = 0$ and $u_6^{(m)} \equiv 0$.

3.4. Surface Screening

Another area of interest when exploring the domain structures of rhombohedral ferroelectrics is the influence of the surface screening charge on their domain structures. Such physical effect in the current work is described by the linear Bardeen screening model and is represented by a term $\epsilon_0 \varphi / \lambda$ in the boundary condition (7) for the Poisson equation. By varying parametric surface screening length λ in this term, we can define strength of the surface screening charges, knowing that the screening is strong when $\lambda \ll 0.1$ nm and weak when $\lambda \gg 0.1$ nm [105].

Weak screening represents defects and impurities on the free surface of a film or charged particles sedimented on the surface. Strong screening, on the other hand, emulates an electrode put on the free surface. Such electrode is not fixed on the film, so that mechanically free conditions still apply for the top surface.

Studying domain structures that form in the presence of surface charges with the screening lengths between 10^{-3} nm and 10 nm, the changes in the domain structure were observed only in the range of λ between 10^{-3} and 10^{-1} nm. Figure 9 shows a comparison of domain structures formed under misfit strains of -2, -0.5, 0, and 1.3 %, which represent all observed polar phases, at strong and weaker surface screening lengths. With gradually changing values of the surface screening length, the domain structure transits smoothly between the two states displayed for each column in the figure. The main feature of the weaker screening is the presence of a closure domain structure underneath the top surface, meaning that the surface screening is too small to compensate the charges, produced by the domains at the top surface, and the structure needs to compensate it by changing itself. The aforementioned changes with an increase of λ are formation, stabilizing and growth of closure domains (Fig. 10). The structure formed under -2% compressive misfit strain exhibits weak closure domains even at the strongest observed screening, which means that, to compensate the domain array in the out-of-plane main phase, the screening must be even larger. Prominent is also that the system is trying to achieve the single-domain state in a film without misfit at the strong surface screening. Even though there remains a disturbance near the bottom surface, the system seems to opt for a single dominant polarization direction. The single-domain state is also one of two alternative meta-stable states for the film with -0.5% compressive misfit strain, another one being a plain two-domain structure with only a tiny hint of closure domains. For the film subject to a tensile misfit (compare Figs. 9.h and 9.d), the changes caused by the surface screening strengthening are rather small. It makes an out-of-plane component more pronounced wherever a remnant domain with such orientation still exists, while the in-plane domains, occupying the vast majority of the bulk, hardly react to the surface screening.

The observed results show a rather predictable behaviour. Just like it was already established for tetragonal structures [88, 89, 97], the main function of surface screening charges is to compensate charges on the free surface generated by out-of-plane domains. Thus, at strong surface screening, there should be no closure domain structures, and it is not uncommon, but rather expected for the film to go for a single-domain structure as a stable or metastable state.

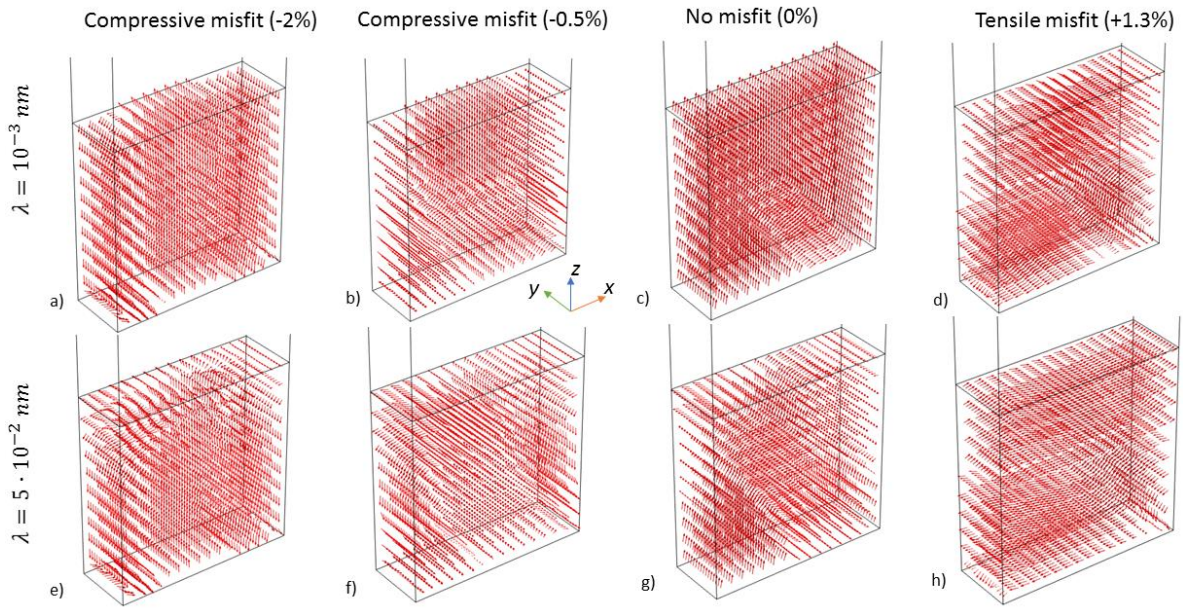


Figure 9. Comparison between domain structures in a thin PZT 60/40 rhombohedral ferroelectric film with varying from left to right misfit strains of -2% (a, e), -0.5% (b, f), 0% (c, g), and +1.3% (d, h) at stronger ($\lambda = 10^{-3} \text{ nm}$) (upper row) and weaker ($\lambda = 5 \cdot 10^{-2} \text{ nm}$) (lower row) surface screening. The computational box has dimensions $h=24 \text{ nm}$, $w=24 \text{ nm}$, $d=8 \text{ nm}$.

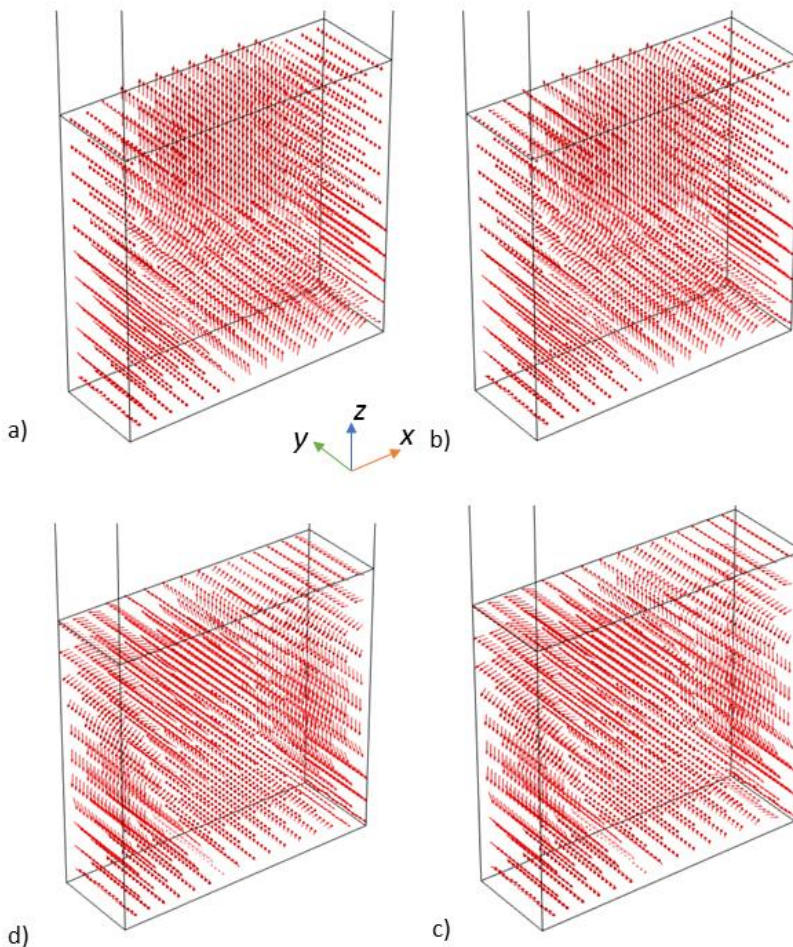


Figure 10. Development of closure domains in a thin ferroelectric film of 60/40 PZT with misfit strain of -0.5% on the bottom surface and screening charge on the top surface with screening length λ of (a) 10^{-3} nm , (b) $2 \times 10^{-3} \text{ nm}$, (c) $1 \times 10^{-2} \text{ nm}$, and (d) $5 \times 10^{-2} \text{ nm}$. The computational box has dimensions $h=24 \text{ nm}$, $w=24 \text{ nm}$, $d=8 \text{ nm}$.

4. Discussion

The performed modelling has shown how the rhombohedral thin ferroelectric films stand out in comparison to e.g. their tetragonal counterparts in terms of phase transformations and electromechanics. Dependent on the misfit strain caused by a substrate, domain structure in such films of PZT 60/40 can contain different types of domain walls and polarization directions in domains that can align by one, two or three components, forming regions with the rhombohedral-like, ac-orthorhombic-like and aa-tetragonal-like polarization patterns. This can be important for the electromechanical properties, because such characteristics like piezocoefficients are influenced by the number of dimensions in which polarization vectors rotate throughout the film volume (Fig. 11). Such characteristic is dependent on strains inside the film, and those can be caused or greatly modified by the mismatch with the substrate. At the detected points of ongoing structural changes (-1% and +1 % uniaxial misfit strains), we also see an increase in the piezocoefficient values, which further supports an idea that they indicate phase transitions. As the rhombohedral ferroelectric films are valued because of their relatively high piezocoefficients, the possibility to control them can be instrumental for electromechanical applications.

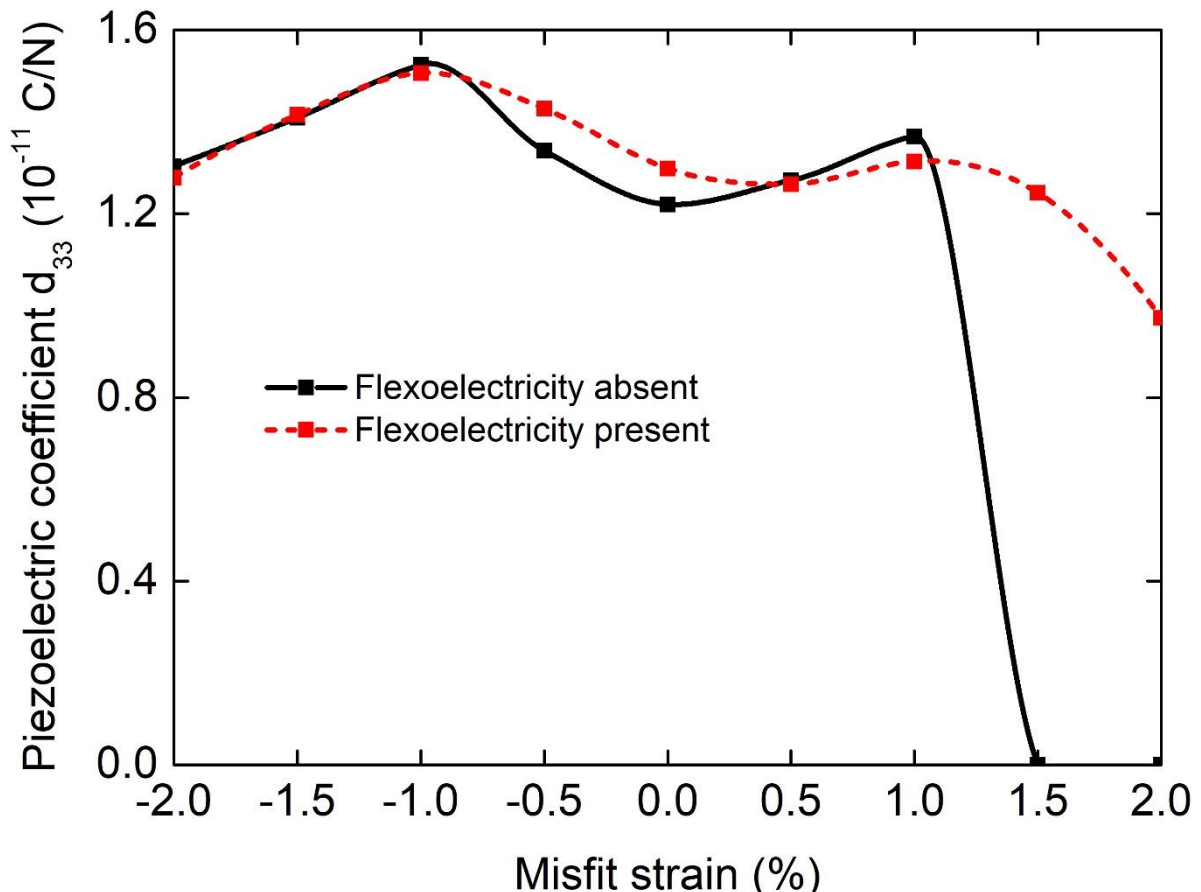


FIGURE 11. Dependence of the piezoelectric coefficient d_{33} of a 24-nm thick PZT 60/40 film on the substrate misfit strain.

The further important finding is the cooperative effect of the misfit strain and flexoelectricity on the ferroelectric phase. It is seen that different values of the misfit strain make either in-plane or out-of-plane orientations of polarization vectors more favourable, which corresponds to the phase diagram for a thin film subject to a uniaxial misfit strain. However, there is a misfit strain range above +1.5% where the polarization disappears if the theory does not account for the flexoelectric effect. Since the nature of flexoelectricity includes turning strain gradients into polarization, and it is known that mismatch strains are a fertile ground for the flexoelectric effect to manifest itself, it can be hypothesized that it is the elastic gradient between the strained bottom of the film and unstrained top that facilitates preserving the polarization.

Comparison of the analytical Landau approach and FEM-LGD results indicates a discrepancy in a misfit-strain dependent phase range. The analytical results for single-domain states (Fig. 8) show the dominance of the in-plane polarization components for all tensile misfit strains, whereas the FEM results (Fig. 5) without accounting for the flexoelectric effect demonstrates that the ferroelectric phase eventually fades away. Even though the in-plane polarization domain structure forms at smaller tensile strains, the bigger tensile strains drive the system into the paraelectric state. This inconsistency can be explained by the structures described by both methods. The analytical LGD approach assumes a single-domain state and does not account for gradient terms that would be necessary to build domain walls, nor does it account for flexoelectricity. Description of a multi-domain state with the FEM LGD provides more complete view at the system, calculates and compares ferro- and paraelectric phase energies more accurately, and results in the polarization disappearance at high tensile strains caused by the substrate. Accounting for the flexoelectric effect supports the polar phase but in a rather exotic in-plane shape.

Surface screening charges influence the domain structure in a predictable way. Similarly to the known cases of tetragonal materials [106, 88, 89, 97], strong screening favours the single-domain structure and suppresses all perturbations. If a misfit strain is applied to the film, achieving the single-domain state is handicapped, but the destruction of closure domains is still predicted for the strong enough screening cases. This, however, counts for the domains with vertical polarization components. When and where the a-domains with only horizontal components are favoured by the strained system, the surface screening has no effect on their structure apart of eliminating small polarization perturbations. This tells us that, similarly to the tetragonal films, surface charges can be used to control domain structures of rhombohedral and, presumably, orthorhombic ferroelectric films.

5. Conclusions

The influence of uniaxial misfit strains, surface charges, and the flexoelectric effect on domain patterns and shape of a thin rhombohedral ferroelectric film was investigated by means of 3D finite element modelling using the Landau-Ginzburg-Devonshire approach. It was observed that spatial distributions of polarization and strain strongly change in dependence on the sign and value of the misfit strain and are crucially conditioned by the presence of the flexoelectric effect. This means that a rhombohedral ferroelectric film can be manipulated into exhibiting different polar and elastic states via the substrate misfit, stabilizing different types of domain structures and deformation patterns. Components of polarization vectors, obtained for each studied misfit strain value, allow for formulating a diagram with structural phases, at 300K,

beginning from the orthorhombic-like structure at higher compressive misfits going through the rhombohedral one around zero misfit into the tetragonal-like at higher tensile misfits. A particular position where the rhombohedral phase is the strongest, as evidenced by polarization vector components and deformation patterns, lies in the interval between -0.5 and 0% of the misfit strain. The flexoelectric effect, considered weak by itself, has a crucial impact on the structure in cases of the tensile misfit strains, as it helps preserve polarization where otherwise it would abruptly disappear. Surface screening charges are seen to be a tool for controlling polar states by their strength, restricted, however, to the cases when polarization has an out-of-plane component.

Acknowledgements

This work was supported by the Deutsche Forschungsgemeinschaft (German Research Society, DFG) via the grant No. 405631895 (GE-1171/8-1). FEM computations for this research were conducted on the Lichtenberg high performance computer of the TU Darmstadt.

Appendix A. Material parameters

A thin film of PZT 60/40 was considered for this investigation. Parameters were predominantly taken from works by Haun, Cross *et al.* [107], Schrade, Xu *et al.* [108], and from the DFT calculations by Völker *et al.* [109]. Table AI shows material parameters considered in the work. Note that the tensor elements are marked using the Voigt notation.

Table AI. Material Parameters of PZT 60/40

Description	Designation	Value	Units
Temperature	T	300	°K
Film thickness	h	24	nm
Ambience layer thickness	h_v	12	nm
Background dielectric permittivity	ε_b	7	dimensionless
Ambience dielectric permittivity	ε_v	1	dimensionless
Surface screening length	λ	>>1	nm
Landau coefficient	α_1	-7.904×10^7	m / F
Landau coefficient	β_{11}	13.69×10^7	$\frac{m^5}{C^2 F}$
Landau coefficient	β_{12}	23.91×10^7	$\frac{m^5}{C^2 F}$
Landau coefficient	γ_{111}	2.713×10^8	$\frac{m^9}{C^4 F}$

Landau coefficient	γ_{112}	12.13×10^8	$\frac{m^9}{C^4 F}$
Landau coefficient	γ_{123}	-56.90×10^8	$\frac{m^9}{C^4 F}$
Gradient term coefficient	g_{11}	15×10^{-11}	m^3 / F
Gradient term coefficient	g_{12}	3.5×10^{-11}	m^3 / F
Gradient term coefficient	g_{44}	6.3×10^{-11}	m^3 / F
Electrostriction coefficient	Q_{11}	7.260×10^{-2}	$\frac{m^4}{C^2}$
Electrostriction coefficient	Q_{12}	-2.708×10^{-2}	$\frac{m^4}{C^2}$
Electrostriction coefficient	Q_{44}	6.293×10^{-2}	$\frac{m^4}{C^2}$
Elastic stiffness coefficient	c_{11}	12×10^{10}	N / m^2
Elastic stiffness coefficient	c_{12}	2.6×10^{10}	N / m^2
Elastic stiffness coefficient	c_{44}	7.5×10^{10}	N / m^2
Elastic compliance coefficient	s_{11}	$\frac{c_{11} + c_{12}}{(c_{11} - c_{12})(c_{11} + 2c_{12})}$	m^2 / N
Elastic compliance coefficient	s_{12}	$\frac{-c_{12}}{(c_{11} - c_{12})(c_{11} + 2c_{12})}$	m^2 / N
Elastic compliance coefficient	s_{44}	$\frac{1}{c_{44}}$	m^2 / N
Flexoelectric coefficient	F_{11}	3×10^{-11}	m^3 / C
Flexoelectric coefficient	F_{12}	1×10^{-11}	m^3 / C
Flexoelectric coefficient	F_{44}	0.5×10^{-11}	m^3 / C
Khalatnikov coefficient	Γ	10^5	$\frac{s \cdot m}{F}$

Appendix B. The LGD analysis of single-domain states of thick and thin films

a. The free energy for a homogeneous polarization

Within the continuous medium Landau-Ginzburg-Devonshire (LGD) approach [110], the value and orientation of the spontaneous polarization P_i in thin ferroelectric films can be controlled

by size effect, temperature T and misfit strain u_m originating from the film-substrate lattice constants mismatch [111]. The density of Gibbs energy, which minimization allows one to calculate the phase diagram for the homogeneous polarization, has the form (see **Appendix C** for derivation):

$$g_L = a_1 P_1^2 + a_2 P_2^2 + a_6 P_1 P_2 + a_3 P_3^2 + a_{11} (P_1^4 + P_2^4) + a_{33} P_3^4 + a_{12} P_1^2 P_2^2 + a_{13} (P_1^2 + P_2^2) P_3^2 + a_{111} (P_1^6 + P_2^6 + P_3^6) + a_{112} [P_1^2 (P_2^4 + P_3^4) + P_2^2 (P_1^4 + P_3^4) + P_3^2 (P_2^4 + P_1^4)] + a_{123} P_1 P_2 P_3^2 \quad (B1)$$

The coefficients:

$$a_1 = \alpha_{1T} (T - T_C^f) - \frac{1}{2} \frac{(u_1^{(m)} + u_2^{(m)})(Q_{11} + Q_{12})}{s_{11} + s_{12}} - \frac{1}{2} \frac{(u_1^{(m)} - u_2^{(m)})(Q_{11} - Q_{12})}{s_{11} - s_{12}}, \quad (B2a)$$

$$a_2 = \alpha_{1T} (T - T_C^f) - \frac{1}{2} \frac{(u_1^{(m)} + u_2^{(m)})(Q_{11} + Q_{12})}{s_{11} + s_{12}} + \frac{1}{2} \frac{(u_1^{(m)} - u_2^{(m)})(Q_{11} - Q_{12})}{s_{11} - s_{12}}, \quad (B2b)$$

$$a_6 = -\frac{u_6^{(m)} Q_{44}}{s_{44}}, \quad a_3 = \alpha_{1T} (T - T_C^f) - \frac{Q_{12} (u_1^{(m)} + u_2^{(m)})}{s_{11} + s_{12}} + \frac{d_{eff}}{2 \varepsilon_0 \varepsilon_f (h + d_{eff})}, \quad (B2c)$$

$$a_{11} = \alpha_{11} + \frac{s_{11} (Q_{11}^2 + Q_{12}^2) - 2 Q_{11} Q_{12} s_{12}}{2 (s_{11}^2 - s_{12}^2)}, \quad a_{33} = \alpha_{11} + \frac{Q_{12}^2}{s_{11} + s_{12}}, \quad (B2d)$$

$$a_{12} = \alpha_{12} - \frac{s_{12} (Q_{11}^2 + Q_{12}^2) - 2 Q_{11} Q_{12} s_{11}}{2 s_{11}^2 - s_{12}^2} + \frac{(Q_{44})^2}{2 s_{44}}, \quad a_{13} = \alpha_{12} + \frac{Q_{12} (Q_{11} + Q_{12})}{s_{11} + s_{12}}. \quad (B2e)$$

Here T_C^f is the Curie temperature of bulk ferroelectric, Q_{ij} are the components of electrostriction tensor, s_{ij} are elastic compliances, $u_1^{(m)}$, $u_2^{(m)}$ and $u_6^{(m)}$ are components of anisotropic mismatch strain. Two diagonal components are determined by the difference of lattice constants in corresponding direction, while $u_6^{(m)}$ is the difference between the corresponding angles of the unit cells of the film and the substrate in the Voight notations. They determine the strain through the conditions at the film-substrate interface for the strain tensor u_{ij} , namely, $u_1 = u_1^{(m)}$ and $u_2 = u_2^{(m)}$, while $u_6 = 2u_6^{(m)}$. The Voight notations are used hereinafter (xx→1, yy→2, zz→3, zy→4, xz→5, xy→6).

The positive coefficient α_T is proportional to the inverse Curie-Weiss constant. When deriving Eq. (B2c) we used the expression for the depolarization field inside the ferroelectric film, $E_3 = -\frac{P_3}{\varepsilon_0 \varepsilon_f} \frac{d_{eff}}{h + d_{eff}}$.

b. Phase diagrams for homogeneous polarization

Phase diagrams of thick and thin $\text{PbZr}_{0.6}\text{Ti}_{0.4}\text{O}_3$ (**PZT**) films with homogeneous polarization in coordinates temperature – mismatch strain, which contain paraelectric (PE) and ferroelectric (FE) phases with out-of-plane (tetragonal FEc phase with $P_3 \neq 0, P_1 = P_2 = 0$),

in-plane (orthorhombic FE aa phase with $P_3 = 0, P_1 = \pm P_2 \neq 0$) and both (rhombohedral FEr phase with $P_3 \neq 0, P_1 = \pm P_2 \neq 0$) orientations of polarization vector are shown in **Figs. B1a-B4a**. The dependence of the in-plane and out-of-plane polarization components on the misfit strain and temperature are shown in **Figs. B1-B4(b-d)**.

The phase designation and classification are taken from papers [16, 17, 71, 76, 112] by Pertsev et al. **Figs. B1-2** are plotted for biaxial misfit strain, $u_1^{(m)} \equiv u_2^{(m)} = u_m$, and so the symmetry of the in-plane polarization direction, $P_1 = \pm P_2$, holds for the strain too. The symmetry $P_1 = \pm P_2$ follows from Eqs. (B2a)-(B2b), which lead to the same expressions for $a_{1,2}$ in the case, namely $a_1 = a_2 = \alpha_{1T}(T - T_C^f) - \frac{u_m(Q_{11}+Q_{12})}{s_{11}+s_{12}}$.

Figs. B3-4 are plotted for uniaxial mismatch strain, $u_1^{(m)} \equiv u_{mX}$, while $u_2^{(m)} = 0$ and $u_6^{(m)} \equiv 0$, so the evident asymmetry $P_1 \neq \pm P_2$, exists for the case. The asymmetry can be explained as follows.

In existing perovskites with $Q_{11} > 0, Q_{12} < 0$, stretching along the x_1 axis corresponding to $u_1^{(m)} > 0$ leads to the appearance and enhancement of the spontaneous polarization component along the same direction, i.e. to an increase in $P_x \equiv P_1$, and its existence at higher temperatures than P_2 . On the contrary, a compression along the x axis, corresponding to $u_1^{(m)} < 0$, leads to suppression and weakening of the spontaneous polarization component along the same direction, i.e. to a decrease in $P_x \equiv P_1$, and its disappearance at lower temperatures compared to P_2 . This effect of "asymmetry" between P_1 and P_2 is clearly seen when comparing **Fig. B3b** with **B3c** plotted for thick films and becomes even more significant for thin films (compare **Fig. B4b** with **B4c**). The asymmetry $P_1 \neq \pm P_2$ follows from Eqs. (B2a)-(B2b), which lead to different expressions for $a_{1,2}$ in the case, namely $a_1 = \alpha_{1T}(T - T_C^f) - \frac{1}{2} \frac{u_{mX}(Q_{11}+Q_{12})}{s_{11}+s_{12}} - \frac{1}{2} \frac{u_{mX}(Q_{11}-Q_{12})}{s_{11}-s_{12}}$, $a_2 = \alpha_{1T}(T - T_C^f) - \frac{1}{2} \frac{u_{mX}(Q_{11}+Q_{12})}{s_{11}+s_{12}} + \frac{1}{2} \frac{u_{mX}(Q_{11}-Q_{12})}{s_{11}-s_{12}}$, and so $a_1 - a_2 = -\frac{u_{mX}(Q_{11}-Q_{12})}{s_{11}-s_{12}}$.

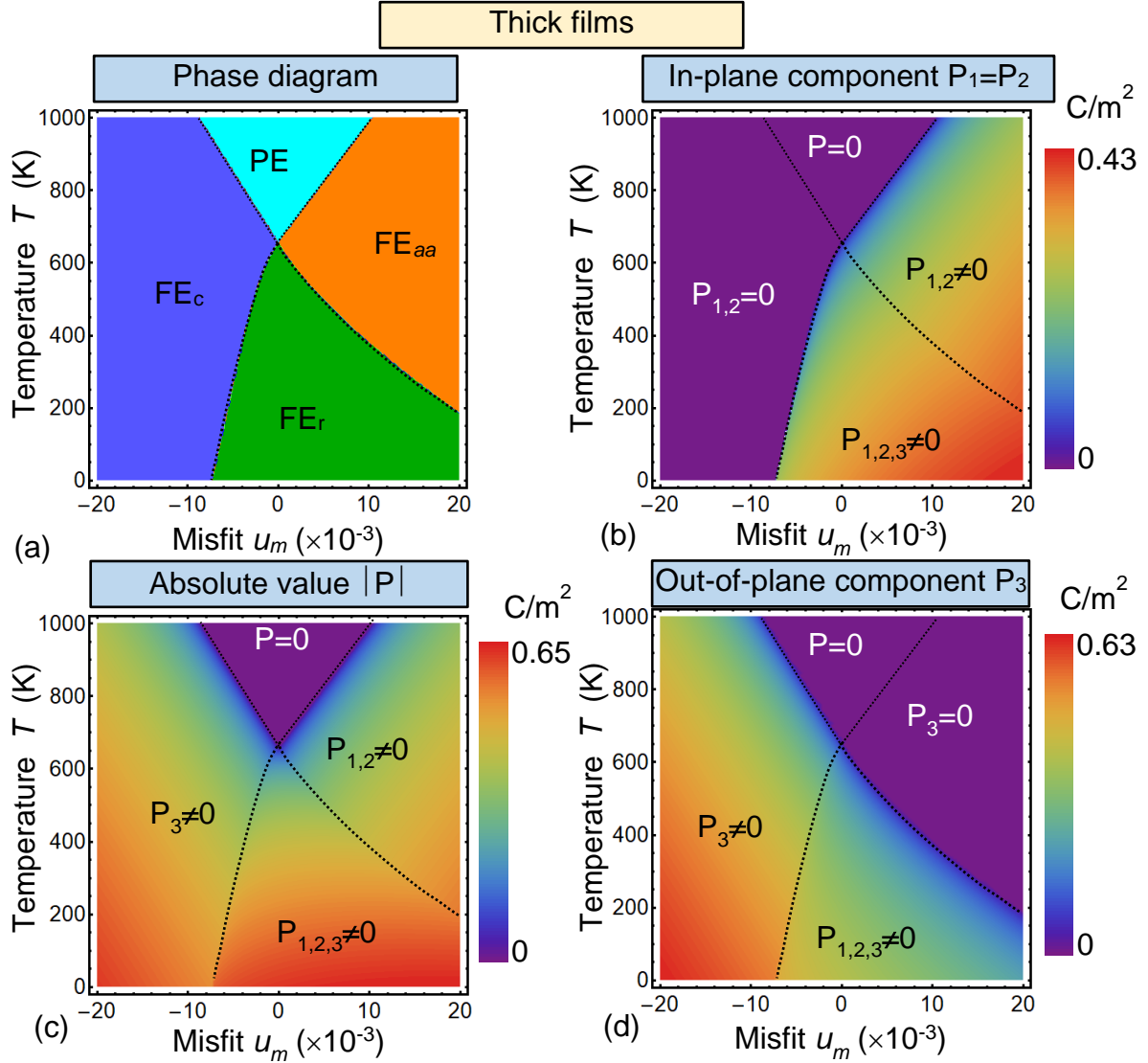


FIGURE B1. (a) Ferroelectric PZT 60/40 phase diagram in coordinates temperature – misfit strain for **thick films**. *Isotropic biaxial* misfit strain between the film and substrate is assumed, $u_1^{(m)} \equiv u_2^{(m)} = u_m$, while $u_6^{(m)} \equiv 0$. Paraelectric phase is denoted as “PE”, while “FE_c”, “FE_a” and “FE_r” show the regions for ferroelectric phases with out-of-plane, in-plane and mixed orientations of polarization, respectively. (b) In-plane and (d) out-of-plane components of polarization along with (c) polarization absolute value dependence on the misfit strain and temperature. Color bars show the range of corresponding values for the contour maps. Film thickness is $h>10^4$ nm and effective spatial gap width is $d_{eff}=0.12$ nm. Bulk parameters are listed in **Table B1**.

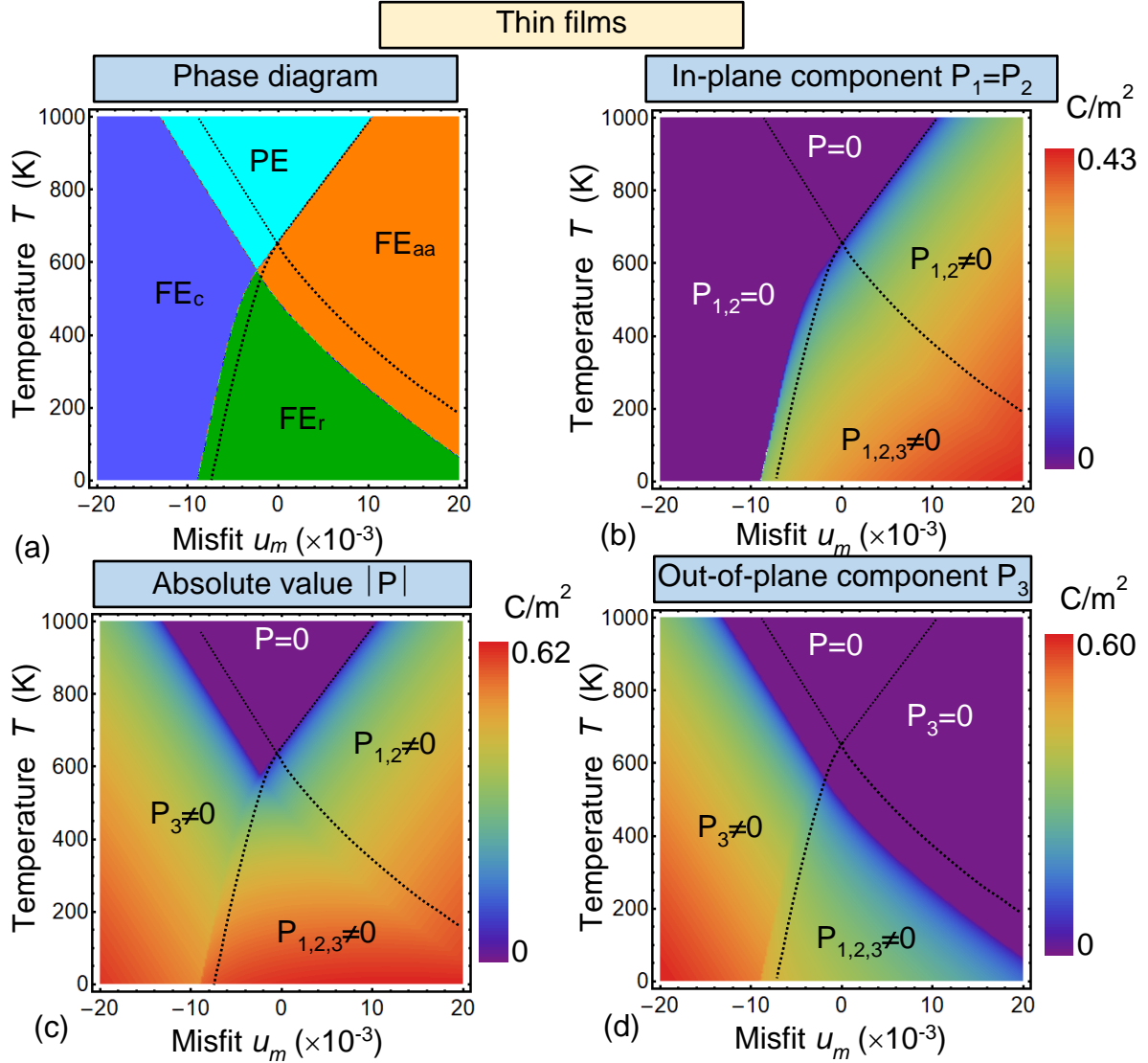


FIGURE B2. (a) Ferroelectric PZT 60/40 phase diagram in coordinates temperature – misfit strain for **thin films**. *Isotropic biaxial* misfit strain between the film and substrate is assumed, $u_1^{(m)} \equiv u_2^{(m)} = u_m$, while $u_6^{(m)} \equiv 0$. Paraelectric phase is denoted as “PE”, while “FE_c”, “FE_a” and “FE_r” show the regions for ferroelectric phases with out-of-plane, in-plane and mixed orientations of polarization, respectively. (b) In-plane and (d) out-of-plane components of polarization along with (c) polarization absolute value dependence on the misfit and temperature. Color bars show the range of corresponding values for the contour maps. Film thickness is $h=24$ nm and effective spatial gap width is $d_{eff}=0.12$ nm. Bulk parameters are listed in **Table BI**.

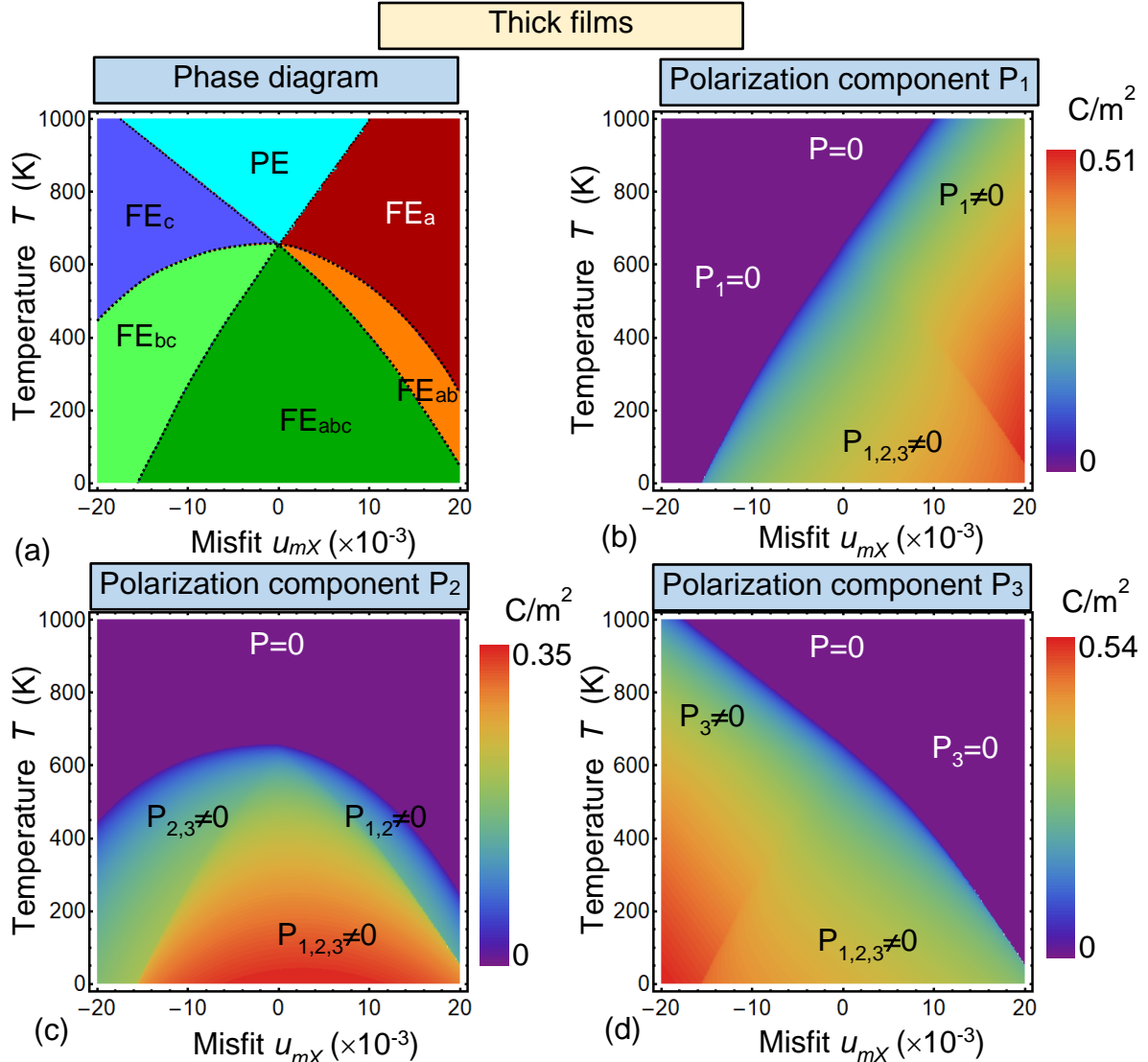


FIGURE B3. (a) Ferroelectric PZT 60/40 phase diagram in coordinates temperature – misfit strain for **thick films**. Anisotropic uniaxial misfit strain between the film and substrate is assumed, $u_1^{(m)} \equiv u_{mx}$, while $u_2^{(m)} = 0$ and $u_6^{(m)} \equiv 0$. Polarization components P_1 (b), P_2 (c) and P_3 (d) dependence on the misfit strain and temperature. Color bars show the range of corresponding values for the contour maps. Paraelectric phase is denoted as “PE”, while “FE_a”, “FE_{ab}”, “FE_{abc}”, “FE_{bc}”, and “FE_c” show the regions for ferroelectric phases with different orientations of polarization, namely, “a” means P_1 , “b” means P_2 and “c” means P_3 . Film thickness is $h > 10^4$ nm and effective spatial gap width is $d_{eff} = 0.12$ nm. Bulk parameters are listed in **Table BI**.

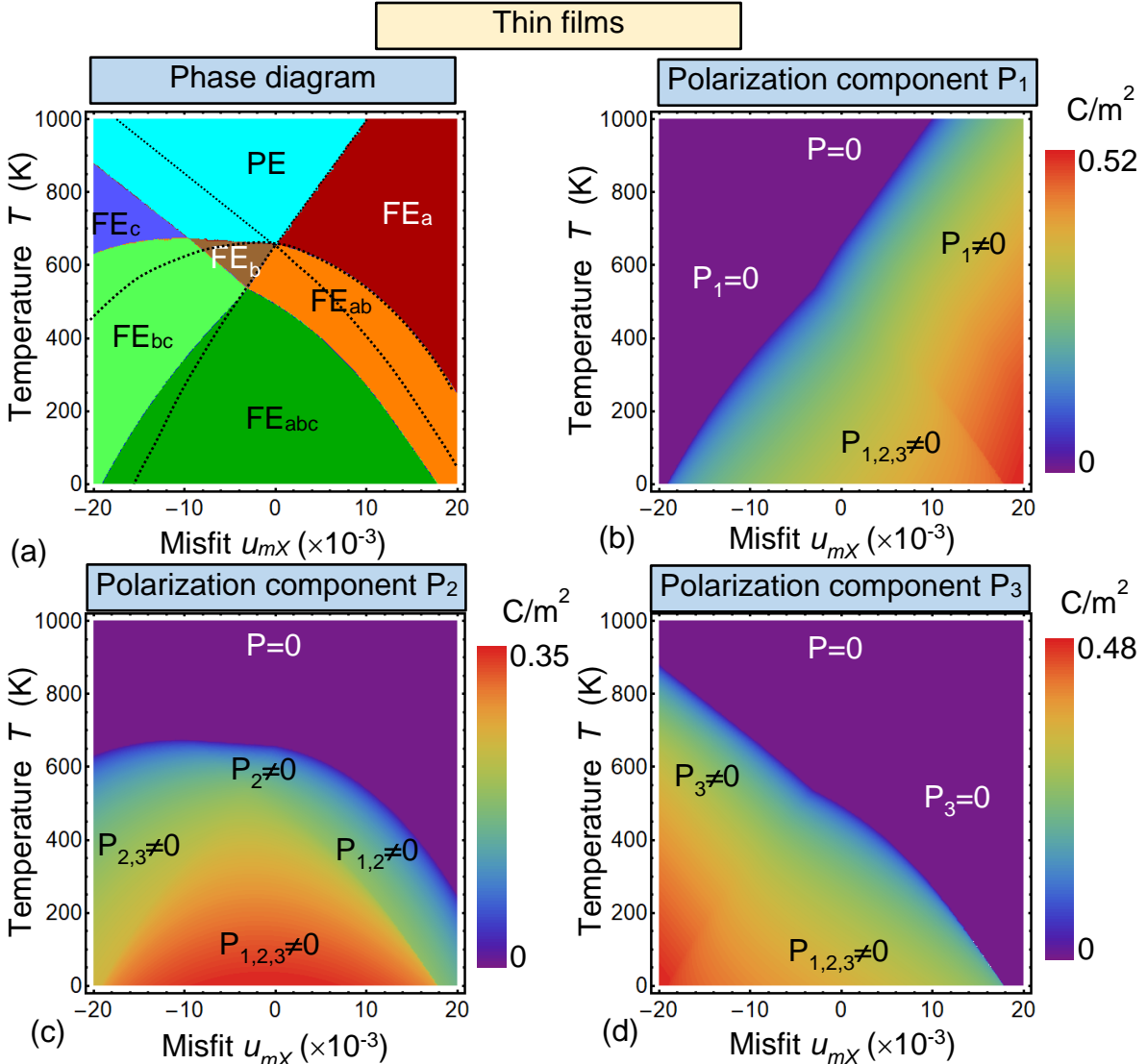


FIGURE B4. (a) Ferroelectric PZT 60/40 phase diagram in coordinates temperature – misfit strain for **thin films**. Anisotropic uniaxial misfit strain between the film and substrate is assumed, $u_1^{(m)} \equiv u_{mx}$, while $u_2^{(m)} = 0$ and $u_6^{(m)} \equiv 0$. Polarization components P_1 (b), P_2 (c) and P_3 (d) dependence on the misfit strain and temperature. Color bars show the range of corresponding values for the contour maps. Paraelectric phase is denoted as “PE”, while “ FE_a ”, “ FE_b ”, “ FE_{ab} ”, “ FE_{abc} ”, “ FE_{bc} ”, and “ FE_c ” show the regions for ferroelectric phases with different orientations of polarization, namely, “a” means P_1 , “b” means P_2 and “c” means P_3 . Film thickness is $h=24$ nm and effective spatial gap width is $d_{eff}=0.12$ nm. Bulk parameters are listed in **Table BI**.

Table BI. Parameters of some compounds of $PbZr_{60}Ti_{40}O_3$ family, used in LGD phenomenological modelling, taken from [107, 112]

parameter	dimensionality	value	Refs.
α_{1T}	$10^5 \text{ m}/(\text{F K})$	2.331	[107]
T_0	°C	364.3	[107]

α_{11}	$10^7 m^5/(F C^2)$	13.62	[107]
α_{12}	$10^8 m^5/(F C^2)$	2.391	[107]
α_{111}	$10^8 m^9/(F C^4)$	2.713	[107]
α_{112}	$10^8 m^9/(F C^4)$	12.13	[107]
α_{123}	$10^9 m^9/(F C^4)$	-5.690	[107]
Q_{11}	$10^2 m^4/C^2$	7.26	[107]
Q_{12}	$10^2 m^4/C^2$	-2.708	[107]
Q_{44}	$10^2 m^4/C^2$	6.293	[107]
s_{11}	10^{-12}Pa^{-1}	8.8	[112]
s_{12}	10^{-12}Pa^{-1}	-2.9	[112]
s_{44}	10^{-12}Pa^{-1}	24.6	[112]

Appendix C. The LGD approach for an anisotropic misfit strain in [001] oriented films (pseudo 4mm symmetry)

The phenomenological Gibbs potential is

$$\begin{aligned}
 \Delta G_{FE} = & a_1^{(P)}(P_1^2 + P_2^2 + P_3^2) + a_{11}^{(P)}(P_1^4 + P_2^4 + P_3^4) + a_{12}^{(P)}(P_1^2 P_2^2 + P_2^2 P_3^2 + P_1^2 P_3^2) + \\
 & a_{111}^{(P)}(P_1^6 + P_2^6 + P_3^6) + a_{112}^{(P)}(P_1^4(P_2^2 + P_3^2) + (P_1^2 + P_3^2)P_2^4 + (P_1^2 + P_2^2)P_3^4) + a_{123}^{(P)}P_1^2 P_2^2 P_3^2 - \\
 & Q_{11}(\sigma_1 P_1^2 + \sigma_2 \overset{\sim}{P_2^2} + \sigma_3 P_3^2) - Q_{12}(\sigma_1 P_2^2 + \sigma_2 P_1^2 + \sigma_1 P_3^2 + \sigma_3 P_1^2 + \sigma_2 P_3^2 + \sigma_3 P_2^2) - \\
 & Q_{44}(\sigma_6 P_1 P_2 + \sigma_5 P_1 P_3 + \sigma_4 P_2 P_3) - \frac{s_{11}}{2}(\sigma_1^2 + \sigma_2^2 + \sigma_3^2) - s_{12}(\sigma_1 \sigma_2 + \sigma_1 \sigma_3 + \sigma_2 \sigma_3) - \\
 & \frac{s_{44}}{2}(\sigma_4^2 + \sigma_5^2 + \sigma_6^2). \quad (C.1)
 \end{aligned}$$

Here we suppose that polarization is homogeneous and neglect the gradient contribution to the energy. Voight matrix notations are used in Eq. (C.1)

$$s_{1111} = s_{11}, \quad s_{1122} = s_{12}, \quad 4s_{1212} = s_{44}, \quad (C.2a)$$

$$Q_{1111} = Q_{11}, \quad Q_{1122} = Q_{12}, \quad 4Q_{1212} = Q_{44}, \quad (C.2b)$$

$$a_{1111}^{(P)} = a_{11}^{(P)}, \quad 6a_{1122}^{(P)} = a_{12}^{(P)}, \quad a_{111111}^{(P)} = a_{111}^{(P)}, \quad 15a_{111122}^{(P)} = a_{112}^{(P)}, \quad 90a_{112233}^{(P)} = a_{123}^{(P)}, \quad (C.2c)$$

$$\sigma_{11} = \sigma_1, \quad \sigma_{22} = \sigma_2, \quad \sigma_{33} = \sigma_3, \quad \sigma_{23} = \sigma_4, \quad \sigma_{13} = \sigma_5, \quad \sigma_{12} = \sigma_6. \quad (C.2d)$$

$$u_{11} = u_1, \quad u_{22} = u_2, \quad u_{33} = u_3, \quad u_{23} = u_4, \quad u_{13} = u_5, \quad u_{12} = u_6. \quad (C.2e)$$

Modified Hooke's law could be obtained from the relation $u_i = -\partial(\Delta G_{FE})/\partial \sigma_i$:

$$u_1 = s_{11}\sigma_1 + s_{12}\sigma_2 + s_{12}\sigma_3 + Q_{11}P_1^2 + Q_{12}P_2^2 + Q_{12}P_3^2 \quad (C.3a)$$

$$u_2 = s_{12}\sigma_1 + s_{11}\sigma_2 + s_{12}\sigma_3 + Q_{12}P_1^2 + Q_{11}P_2^2 + Q_{12}P_3^2 \quad (C.3b)$$

$$u_3 = s_{12}\sigma_1 + s_{12}\sigma_2 + s_{11}\sigma_3 + Q_{12}P_1^2 + Q_{12}P_2^2 + Q_{11}P_3^2 \quad (C.3c)$$

$$u_4 = s_{44}\sigma_4 + Q_{44}P_2 P_3 \quad (C.3d)$$

$$u_5 = s_{44}\sigma_5 + Q_{44}P_1 P_3 \quad (C.3e)$$

$$u_6 = s_{44}\sigma_6 + Q_{44}P_1P_2 \quad (C.3f)$$

The solution for the misfit of a thin film with its substrate is well known. For the film with the normal along x_3 direction one has the following relations for stress and strain components (see e.g. [16]):

$$\sigma_4 = \sigma_5 = \sigma_6 = 0 \quad (C.4a)$$

$$u_1 = u_1^{(m)}, \quad u_2 = u_2^{(m)}, \quad u_6 = u_6^{(m)} \quad (C.4b)$$

Here the definitions of misfit strain components $u_1^{(m)}$, $u_2^{(m)}$ and $u_6^{(m)}$ are given after Eqs.(B.2e). Taking (C.3) and (C.4) into account

$$u_1^{(m)} = s_{11}\sigma_1 + s_{12}\sigma_2 + Q_{11}P_1^2 + Q_{12}P_2^2 + Q_{12}P_3^2 \quad (C.5a)$$

$$u_2^{(m)} = s_{12}\sigma_1 + s_{11}\sigma_2 + Q_{12}P_1^2 + Q_{11}P_2^2 + Q_{12}P_3^2 \quad (C.5b)$$

$$u_3 = s_{12}\sigma_1 + s_{12}\sigma_2 + Q_{12}P_1^2 + Q_{12}P_2^2 + Q_{11}P_3^2 \quad (C.5c)$$

$$u_4 = Q_{44}P_2P_3, \quad u_5 = Q_{44}P_1P_3, \quad u_6^{(m)} = s_{44}\sigma_6 + Q_{44}P_1P_2. \quad (C.5d)$$

The solution of the system (C.5) is

$$\sigma_1 = \frac{s_{11}\delta u_1 - s_{12}\delta u_2}{s_{11}^2 - s_{12}^2} \equiv \frac{1}{2} \left(\frac{\delta u_1 + \delta u_2}{s_{11} + s_{12}} + \frac{\delta u_1 - \delta u_2}{s_{11} - s_{12}} \right), \quad (C.6a)$$

$$\sigma_2 = \frac{s_{11}\delta u_2 - s_{12}\delta u_1}{s_{11}^2 - s_{12}^2} \equiv \frac{1}{2} \left(\frac{\delta u_1 + \delta u_2}{s_{11} + s_{12}} - \frac{\delta u_1 - \delta u_2}{s_{11} - s_{12}} \right), \quad (C.6b)$$

$$u_3 = s_{12} \frac{\delta u_1 + \delta u_2}{s_{11} + s_{12}} + Q_{12}P_1^2 + Q_{12}P_2^2 + Q_{11}P_3^2, \quad (C.6c)$$

$$\sigma_6 = \frac{u_6^{(m)} - Q_{44}P_1P_2}{s_{44}}, \quad u_4 = Q_{44}P_2P_3, \quad u_5 = Q_{44}P_1P_3. \quad (C.6d)$$

Here we introduce values δu_1 and δu_2 as the differences between misfit and spontaneous strain components.

$$\delta u_1 = u_1^{(m)} - Q_{11}P_1^2 - Q_{12}P_2^2 - Q_{12}P_3^2, \quad (C.6e)$$

$$\delta u_2 = u_2^{(m)} - Q_{12}P_1^2 - Q_{11}P_2^2 - Q_{12}P_3^2, \quad (C.6f)$$

Finally, the Legendre transformation of the expression (C.1) for Gibbs potential gives us the Helmholtz free energy:

$$\begin{aligned} \widetilde{\Delta F}_{FE} = \Delta G_{FE} + \sigma_1 u_1 + \sigma_2 u_2 + \sigma_6 u_6 &= a_1^{(P)}(P_1^2 + P_2^2 + P_3^2) + a_{11}^{(P)}(P_1^4 + P_3^4) + \\ &+ a_{12}^{(P)}(P_1^2 P_2^2 + P_1^2 P_3^2 + P_2^2 P_3^2) + a_{111}^{(P)}(P_1^6 + P_3^6) + a_{112}^{(P)}(P_1^4 P_3^2 + P_1^2 P_3^4) - Q_{11}(\sigma_1 P_1^2 + \\ &+ \sigma_{22} P_2^2) - Q_{12}(\sigma_1(P_2^2 + P_3^2) + \sigma_2(P_1^2 + P_3^2)) - Q_{44}\sigma_4 P_1 P_2 - \frac{s_{11}}{2}(\sigma_1^2 + \sigma_2^2) - s_{12}\sigma_1\sigma_2 - \\ &- \frac{s_{44}}{2}\sigma_6^2 + \sigma_1 u_1^{(m)} + \sigma_2 u_2^{(m)} + \sigma_6 u_6^{(m)}, \end{aligned} \quad (C.7a)$$

where an “elastic” part of (C.7a) can be transformed as follows,

$$\begin{aligned}
& -Q_{11}(\sigma_1 P_1^2 + \sigma_2 P_2^2) - Q_{12}(\sigma_1(P_2^2 + P_3^2) + \sigma_2(P_1^2 + P_3^2)) - Q_{44}\sigma_6 P_1 P_2 - \frac{s_{11}}{2}(\sigma_1^2 + \sigma_2^2) - \\
& s_{12}\sigma_1\sigma_2 - \frac{s_{44}}{2}\sigma_6^2 + \sigma_1 u_1^{(m)} + \sigma_2 u_2^{(m)} = \sigma_1 \delta u_1 + \sigma_2 \delta u_2 - \frac{s_{11}}{2}(\sigma_1^2 + \sigma_2^2) - s_{12}\sigma_1\sigma_2 - \\
& \frac{s_{44}}{2}\sigma_6^2 + \sigma_{12}(u_6^{(m)} - Q_{44}P_1 P_2) = \frac{(\sigma_1 + \sigma_2)(\delta u_1 + \delta u_2)}{2} + \frac{(\sigma_1 - \sigma_2)(\delta u_1 - \delta u_2)}{2} - \frac{(s_{11} + s_{12})}{4}(\sigma_1 + \sigma_2)^2 - \\
& \frac{(s_{11} - s_{12})}{4}(\sigma_1 - \sigma_2)^2 + \frac{(u_6^{(m)} - Q_{44}P_1 P_2)^2}{2s_{44}} = \frac{(\delta u_1 + \delta u_2)^2}{4(s_{11} + s_{12})} + \frac{(\delta u_1 - \delta u_2)^2}{4(s_{11} - s_{12})} + \frac{(u_6^{(m)} - Q_{44}P_1 P_2)^2}{2s_{44}} = \\
& \frac{(u_1^{(m)} + u_2^{(m)} - (Q_{11} + Q_{12})(P_1^2 + P_2^2) - 2Q_{12}P_3^2)^2}{4(s_{11} + s_{12})} + \frac{(u_1^{(m)} - u_2^{(m)} - (Q_{11} - Q_{12})(P_1^2 - P_2^2))^2}{4(s_{11} - s_{12})} + \frac{(u_6^{(m)} - Q_{44}P_1 P_2)^2}{2s_{44}}
\end{aligned} \tag{C.7b}$$

After all, the free energy due to misfit strain acquires the form

$$\begin{aligned}
\widetilde{\Delta F}_{FE} = & \frac{(u_1^{(m)} + u_2^{(m)})^2}{4(s_{11} + s_{12})} + \frac{(u_1^{(m)} - u_2^{(m)})^2}{4(s_{11} - s_{12})} + \frac{(u_6^{(m)})^2}{2s_{44}} + \left(a_1^{(P)} - \frac{1}{2} \frac{(u_1^{(m)} + u_2^{(m)})(Q_{11} + Q_{12})}{s_{11} + s_{12}} - \right. \\
& \left. \frac{1}{2} \frac{(u_1^{(m)} - u_2^{(m)})(Q_{11} - Q_{12})}{s_{11} - s_{12}} \right) P_1^2 + \left(a_1^{(P)} - \frac{1}{2} \frac{(u_1^{(m)} + u_2^{(m)})(Q_{11} + Q_{12})}{s_{11} + s_{12}} + \frac{1}{2} \frac{(u_1^{(m)} - u_2^{(m)})(Q_{11} - Q_{12})}{s_{11} - s_{12}} \right) P_2^2 - \\
& \frac{u_6^{(m)} Q_{44}}{s_{44}} P_1 P_2 + \left(a_1^{(P)} - \frac{(u_1^{(m)} + u_2^{(m)}) Q_{12}}{s_{11} + s_{12}} \right) P_3^2 + \left(a_{11}^{(P)} + \frac{1}{4} \frac{(Q_{11} + Q_{12})^2}{s_{11} + s_{12}} + \frac{1}{4} \frac{(Q_{11} - Q_{12})^2}{s_{11} - s_{12}} \right) (P_1^4 + P_2^4) + \\
& \left(a_{11}^{(P)} + \frac{(Q_{12})^2}{s_{11} + s_{12}} \right) P_3^4 + \left(a_{12}^{(P)} + \frac{1}{2} \frac{(Q_{11} + Q_{12})^2}{s_{11} + s_{12}} - \frac{1}{2} \frac{(Q_{11} - Q_{12})^2}{s_{11} - s_{12}} + \frac{(Q_{44})^2}{2s_{44}} \right) P_1^2 P_2^2 + \left(a_{12}^{(P)} + \right. \\
& \left. \frac{(Q_{11} + Q_{12}) Q_{12}}{s_{11} + s_{12}} \right) (P_1^2 + P_2^2) P_3^2 + a_{111}^{(P)} (P_1^6 + P_2^6 + P_3^6) + a_{112}^{(P)} (P_1^4 (P_2^2 + P_3^2) + (P_1^2 + P_3^2) P_2^4 + \\
& (P_1^2 + P_2^2) P_3^4) + a_{123}^{(P)} P_1^2 P_2^2 P_3^2
\end{aligned} \tag{C.8}$$

Analysis of the coefficients before P_i^2 , $P_1 P_2$, $P_i^2 P_j^2$, and P_i^4 , leads to Eqs. (B.2).

References

- 1 H. Jaffe, Titanate Ceramics for Electromechanical Purposes, *Ind. Eng. Chem.* 42, 264-268 (1950).
- 2 J. Carrano, J. Lee, Electrical and Reliability Properties of PZT Thin Films for USLI DRAM Applications, *IEEE Transactions on Ultrasonics, Ferroelectrics, and Frequency Control* 38, 6, 690-703 (1991).
- 3 G.D. Shilpa, K. Sreelakshmi and M.G. Ananthaprasad, PZT thin film deposition techniques, properties and its application in ultrasonic MEMS sensors: a review, *IOP Conf. Ser.: Mater. Sci. Eng.* 149, 012190 (2016).
- 4 D.F. Bahr, J.C. Merillo, P. Banerjee, C.M. Yip, Reliability and Properties of Pzt Thin Films for Mems Applications, *MRS Proceedings*, 546, 153 (1998).
- 5 N. Setter, D. Damjanovic, L. Eng, G. Fox, S. Gevorgian, S. Hong, A. Kingon et al., Ferroelectric thin films: Review of materials, properties, and applications, *J. Appl. Phys.* 100, no. 5, 051606 (2006).
- 6 A.K. Tagantsev, L.E. Cross, J. Fousek, Domains in Ferroic Crystals and Thin Films, Springer, Dordrecht (2010).

7 J. Ouyang, Nanostructures in Ferroelectric Films for Energy Applications: Domains, Grains, Interfaces and Engineering Methods, Elsevier (2019).

8 M.J. Haun, Z.Q. Zhuang, E. Furman, S.J. Jang, L.E. Cross, Thermodynamic theory of the lead zirconate-titanate solid solution system, part III: Curie constant and sixth-order polarization interaction dielectric stiffness coefficients, *Ferroelectrics* 99, 45-54 (1989).

9 D.S.L. Pontes, L. Garcia, F.M. Pontes, A. Beltrán, J. Andrés and E. Longo, Synthesis, optical and ferroelectric properties of PZT thin films: experimental and theoretical investigation, *J. Mater. Chem.* 22, 6587 (2012).

10 G. Tan, K. Maruyama, Y. Kanamisu, S. Nishioka, T. Ozaki, T. Umegaki, H. Hida & I. Kanno, Crystallographic contributions to piezoelectric properties in PZT thin films, *Sci. Rep.* 9, 7309 (2019).

11 G. Lu, H. Dong, J. Chen, J. Cheng, Enhanced dielectric and ferroelectric properties of PZT thin films derived by an ethylene glycol modified sol-gel method, *J. Sol-Gel Sci. Technol.* 82, 530-535 (2017).

12 M. Toyama, R. Kubo, E. Takata, K. Tanaka, K. Ohwada, Characterization of piezoelectric properties of PZT thin films deposited on Si by ECR sputtering, *Sensors and Actuators A* 45, 125-129 (1994).

13 N. Setter, D. Damjanovic, L. Eng, G. Fox, S. Gevorgian, S. Hong, A. Kingon, H. Kohlstedt, N. Park, G.B. Stephenson, I. Stolichnov, A.K. Tagantsev, D.V. Taylor, T. Yamada, S. Streiffer, Ferroelectric thin films: Review of materials, properties and applications, *J. Appl. Phys.* 100, 051606 (2006).

14 D. Das, L. Sanchez, J. Martin, B. Power, S. Isaacson, R.G. Polcawich, and I. Chasiotis, Control of mechanical response of freestanding PbZr0.52Ti0.48O3 films through texture, *Appl. Phys. Lett.* 109, no. 13, 131905 (2016).

15 P. Gerber, U. Böttger, R. Waser, Composition influences on the electrical and electromechanical properties of lead zirconate-titanate thin films, *J. Appl. Phys.* 100, 124105-1-8 (2006).

16 N.A. Pertsev, A.G. Zembilgotov, and A.K. Tagantsev, Effect of Mechanical Boundary Conditions on Phase Diagrams of Epitaxial Ferroelectric Films, *Phys. Rev. Lett.* 80, 1988 (1998).

17 N.A. Pertsev, A.G. Zembilgotov, Ferroelectric thin films grown on tensile substrates: Renormalization of the Curie-Weiss law and apparent absence of ferroelectricity, *J. Appl. Phys.* 85, 1698 (1999).

18 S.K. Streiffer, C.B. Parker, A.E. Romanov, M.J. Lefevre, L. Zhao, J.S. Speck, W. Pompe, C.M. Foster, G.R. Bai, Domain patterns in epitaxial rhombohedral ferroelectric films. I. Geometry and experiments, *J. Appl. Phys.* 83, 2742-2753 (1998).

19 Y.L. Li, S.Y. Hu, L.Q. Chen, Ferroelectric domain morphologies of (001) PbZr_{1-x}Ti_xO₃ epitaxial thin films, *J. Appl. Phys.* 97, 034112 (2005).

20 Y. Wei, P. Nukala, M. Salverda, S. Matzen, H.J. Zhao, J. Momand, A.S. Everhardt, G. Agnus, G.R. Blake, P. Lecoeur, B.J. Kooi, J. Íñiguez, B. Dkhil, B. Noheda, A rhombohedral ferroelectric phase in epitaxially strained Hf_{0.5}Zr_{0.5}O₂ thin films, *Nature Materials* 17, 1095-1100 (2018).

21 M.P. Cruz, Y.H. Chu, J.X. Zhang, P.L. Yang, F. Zavaliche, Q. He, P. Shafer, L.Q. Chen, R. Ramesh, Strain Control of Domain-Wall Stability in Epitaxial BiFeO₃ (110) Films, *Phys. Rev. Lett.* 99, 217601 (2007).

22 P. Zubko, G. Catalan, A.K. Tagantsev, Flexoelectric Effect in Solids, *Ann. Rev. Mat. Res.* 43, 387-421, (2013).

23 M.J. Zou, Y.L. Tang, Y.L. Zhu, Y.J. Wang, Y.P. Feng, M.J. Han, N.B. Zhang, J.Y. Ma, W.R. Geng, W.W. Hu, X.W. Guo, B. Wu, X.L. Ma, Flexoelectricity-induced retention failure in ferroelectric films, *Acta Mat.* 196, 61-68 (2020).

24 W. Cao, G.R. Barsch, Landau-Ginzburg model of interphase boundaries in improper ferroelastic perovskites of d418 h symmetry, *Phys. Rev. B* 41, 4334–48 (1990).

25 A.N. Morozovska, E.A. Eliseev, M.D. Glinchuk, L.-Q. Chen, V. Gopalan, Interfacial polarization and pyroelectricity in antiferrodistortive structures induced by a flexoelectric effect and rotostriction, *Phys. Rev. B* 85, 094107 (2012).

26 S.V. Kalinin, A.N. Morozovska, Focusing light on flexoelectricity, *Nature Nanotechnology* 10, 916-917 (2015).

27 G. Catalan, B. Noheda, J. McAneney, L.J. Sinnamon, J.M. Gregg, Strain gradients in epitaxial ferroelectrics, *Phys. Rev. B* 72, 020102 (2005).

28 H.J. Kim, S. Hoon Oh, H.M. Jang, Thermodynamic theory of stress distribution in epitaxial Pb(Zr,Ti)O₃ thin films, *Appl. Phys. Lett.* 75(20), 3195–97 (1999).

29 G. Catalan, L.J. Sinnamon, J.M. Gregg, The effect of flexoelectricity on the dielectric properties of inhomogeneously strained ferroelectric thin films, *J. Phys. Condens. Matter* 16(13), 2253 (2004).

30 M.S. Majdoub, R. Maranganti, P. Sharma, Understanding the origins of the intrinsic dead layer effect in nanocapacitors. *Phys. Rev. B* 79, 115412 (2009).

31 L.J. Sinnamon, R.W. Bowman, J.M. Gregg, Investigation of dead-layer thickness in SrRuO₃/Ba0.5Sr0.5TiO₃/Au thin-film capacitors, *Appl. Phys. Lett.* 78(12) 1724–26 (2001).

32 H. Zhou, J. Hong, Y. Zhang, F. Li, Y. Pei, D. Fang, Flexoelectricity induced increase of critical thickness in epitaxial ferroelectric thin films, *J. Phys. Condens. Matter* 407(17) 3377–81 (2012).

33 G. Catalan, J. Seidel, R. Ramesh, J.F. Scott, Domain wall nanoelectronics. *Rev. Mod. Phys.* 84, 119–56 (2012).

34 J. Seidel, L.W. Martin, Q. He, Q. Zhan, Y.H. Chu, A. Rother, M.E. Hawkridge, P. Maksymovych, P. Yu, M. Gajek, N. Balke, S.V. Kalinin, S. Gemming, F. Wang, G. Catalan, J.F. Scott, N.A. Spaldin, J. Orenstein, R. Ramesh, Conduction at domain walls in oxide multiferroics, *Nat. Mater.* 8, 229–34 (2009).

35 A.R. Damodaran, E. Breckenfeld, Z. Chen, S. Lee and L.W. Martin, Enhancement of Ferroelectric Curie Temperature in BaTiO₃ Films via Strain-Induced Defect Dipole Alignment, *Adv. Mater.* 26, 6341 (2014).

36 R.V.K. Mangalam, J. Karthik, A.R. Damodaran, J.C. Agar and L.W. Martin, Unexpected Crystal and Domain Structures and Properties in Compositionally Graded PbZr_{1-x}Ti_xO₃ Thin Films, *Adv. Mater.* 25, 1761 (2013).

37 D. Lee, A. Yoon, S.Y. Jang, J.-G. Yoon, J.-S. Chung, M. Kim, J.F. Scott and T.W. Noh, Giant Flexoelectric Effect in Ferroelectric Epitaxial Thin Films, *Phys. Rev. Lett.* 107, 057602 (2011).

38 D. Lee, B.C. Jeon, A. Yoon, Y.J. Shin, M.H. Lee, T.K. Song, S.D. Bu, M. Kim, J.-S. Chung, J.-G. Yoon, T.W. Noh, Flexoelectric Control of Defect Formation in Ferroelectric Epitaxial Thin Films, *Adv. Mater.* 26, 5005 (2014).

39 E.V. Bursian, Z. Oi, K.V. Makarov, Ferroelectric plate polarization by bending, *Izv. Akad. Nauk SSSR Ser. Fiz.* 33(7), 1098–102 (1969).

40 H. Lu, C.-W. Bark, D. Esque de los Ojos, J. Alcala, C.B. Eom, G. Catalan, A. Gruverman, Mechanical writing of ferroelectric polarization. *Science* 336(6077), 59–61 (2012).

41 A. Gruverman, B.J. Rodriguez, A.I. Kingon, R.J. Nemanich, A.K. Tagantsev, J.S. Cross, M. Tsukada, Mechanical stress effect on imprint behavior of integrated ferroelectric capacitors. *Appl. Phys. Lett.* 83(4), 728–30 (2003).

42 G. Catalan, A. Lubk, A.H.G. Vlooswijk, E. Snoeck, C. Magen, A. Janssens, G. Rispens, G. Rijnders, D.H.A. Blank, B. Noheda, Flexoelectric rotation of polarization in ferroelectric thin films, *Nat. Mater.* 10, 963 (2011).

43 E.V. Bursian, O.I. Zaikovskii, Changes in the curvature of a ferroelectric film due to polarization, *Sov. Phys. Solid State* 10(5), 1121–24 (1968).

44 J.D. Axe, J. Harada, G. Shirane, Anomalous acoustic dispersion in centrosymmetric crystals with soft optic phonons, *Phys. Rev. B* 1, 1227–34 (1970).

45 J.W. Matthews, A.E. Blakeslee, Defects in epitaxial multilayers. I. Misfit dislocations, *J. Cryst. Growth* 27, 118–25 (1974).

46 A. Damodaran, J.C. Agar, S. Pandya, Z. Chen, L. Dedon, R. Xu, B. Apgar, S. Saremi, L.W. Martin, New modalities of strain-control of ferroelectric thin films, *J. Phys.: Condens. Matter* 28, 263001 (2016).

47 J. Schwarzkopf, D. Braun, M. Hanke, R. Uecker and M. Schmidbauer, Strain Engineering of Ferroelectric Domains in $K_xNa_{1-x}NbO_3$ Epitaxial Layers, *Frontiers in Materials* 4, 00026 (2017).

48 L. von Helden, L. Bogula, P.-E. Janolin, M. Hanke, T. Breuer, M. Schmidbauer, S. Ganschow, and J. Schwarzkopf, Huge impact of compressive strain on phase transition temperatures in epitaxial ferroelectric $K_xNa_{1-x}NbO_3$ thin films, *Appl. Phys. Lett.* 114, 232905 (2019).

49 M. Schmidbauer, D. Braun, T. Markurt, M. Hanke and J. Schwarzkopf, Strain engineering of monoclinic domains in $K_xNa_{1-x}NbO_3$ epitaxial layers: a pathway to enhanced piezoelectric properties, *Nanotechnology* 28, 24LT02 (2017).

50 D. Braun, M. Schmidbauer, M. Hanke, A. Kwasniewski, and J. Schwarzkopf, Tunable ferroelectric domain wall alignment in strained monoclinic $K_xNa_{1-x}NbO_3$ epitaxial films, *Appl. Phys. Lett.* 110, 232903 (2017).

51 D. Braun, M. Schmidbauer, M. Hanke, and J. Schwarzkopf, Hierarchy and scaling behaviour of multi-rank domain patterns in ferroelectric $K_{0.9}Na_{0.1}NbO_3$ strained films, *Nanotechnology* 29, 015701 (2018).

52 D. Sando, A. Barthélémy and M. Bibes, $BiFeO_3$ epitaxial thin films and devices: past, present and future, *J. Phys.: Condens. Matter* 26, 473201 (2014).

53 R.J. Zeches, M.D. Rossell, J.X. Zhang, A.J. Hatt, Q. He, C.-H. Yang, A. Kumar, C.H. Wang, A. Melville, C. Adamo, G. Sheng, Y.-H. Chu, J.F. Ihlefeld, R. Erni, C. Ederer, V. Gopalan, L.Q. Chen, D.G. Schlom, N.A. Spaldin, L.W. Martin, R. Ramesh, A Strain-Driven Morphotropic Phase Boundary in $BiFeO_3$, *Science* 326, 977-980 (2009).

54 Y. Saito, H. Takao, T. Tani, T. Nonoyama, K. Takatori, T. Homma, T. Nagaya & Masaya Nakamura, Lead-free piezoceramics, *Nature* 432 84-87 (2004).

55 V. Nagarajan, S. Prasertchoung, T. Zhao, H. Zheng, J. Ouyang, and R. Ramesh, Size effects in ultrathin epitaxial ferroelectric heterostructures, *Appl. Phys. Lett.* 84, 5225 (2004).

56 A. J. Hatt, N.A. Spaldin, and C. Ederer, Strain-induced isosymmetric phase transition in $BiFeO_3$, *Phys. Rev. B* 81, 054109 (2010).

57 D.G. Schlom, L.-Q. Chen, X. Pan, A. Schmehl, M.A. Zurbuchen, A Thin Film Approach to Engineering Functionality into Oxides, *J. Am. Ceram. Soc.* 91, 2429-2454 (2008).

58 D.G. Schlom, L.-Q. Chen, C.-B. Eom K.M. Rabe, S.K. Streiffer, and J.-M. Triscone, Strain Tuning of Ferroelectric Films, *Annu. Rev. Mat. Res.* 37, 589-626 (2007).

59 J.H. Haeni, P. Irvin, W. Chang, R. Uecker, P. Reiche, Y.L. Li, S. Choudhury, W. Tian, M.E. Hawley, B. Craig, A.K. Tagantsev, X.Q. Pan, S.K. Streiffer, L.Q. Chen, S.W. Kirchoefer, J. Levy & D.G. Schlom, Room-temperature ferroelectricity in strained $SrTiO_3$, *Nature* 430, 758-761 (2004).

60 K.J. Choi, M. Biegalski, Y.L. Li, A. Sharan, J. Schubert, R. Uecker, P. Reiche, X.B. Chen, X.Q. Pan, V. Gopalan, L.-Q. Chen, D.G. Schlom, C.B. Eom, Enhancement of Ferroelectricity in Strained BaTiO₃, *Science* 306, 1005-1009 (2004).

61 M.D. Biegalski, Y. Jia, D.G. Schlom, S. Troiler-McKinstry, S.K. Streiffer, V. Sherman, R. Uecker, and P. Reiche, Relaxor ferroelectricity in strained epitaxial SrTiO₃ thin films on DyScO₃ substrates, *Appl. Phys. Lett.* 88, 192907 (2006).

62 M.J. Zou, Y.L. Tang, Y.L. Zhu, Y.P. Feng, Y.J. Wang, M.J. Han, N.B. Zhang, J.Y. Ma, B. Wu, X.L. Ma, Anisotropic strain: A critical role in domain evolution in (111)- Oriented ferroelectric films, *Acta Mat.* 166, 503-511 (2019).

63 Y. Wei, P. Nukala, M. Salverda, S. Matzen, H.J. Zhao, J. Mommand, A.S. Everhardt, G. Agnus, G.R. Blake, P. Lecoeur, B.J. Kooi, J. Íñiguez, B. Dkhil, B. Noheda, A rhombohedral ferroelectric phase in epitaxially strained Hf_{0.5}Zr_{0.5}O₂ thin films, *Nat. Mat.* 17, 1095-1100 (2018).

64 Dragan Damjanovic, Ferroelectric, dielectric and piezoelectric properties of ferroelectric thin films and ceramics, *Rep. Prog. Phys.* 61, 1267 (1998).

65 Y. Xu, Ferroelectric Materials and Their Applications, Elsevier Amsterdam (2013).

66 S. Wada, T. Muraishi, K. Yokoh, K. Yako, H. Kamemoto & T. Tsurumi, Domain Wall Engineering in Lead-Free Piezoelectric Crystals, *Ferroelectrics* 355, 37-49 (2007).

67 D.-J. Kim, J.-P. Maria, and A. I. Kingon, Evaluation of intrinsic and extrinsic contributions to the piezoelectric properties of Pb(Zr_{1-x}Ti_x)O₃ thin films as a function of composition, *J. Appl. Phys.* 93, 5568 (2003).

68 V. Nagarajan, A. Roytburd, A. Stanishevsky, S. Prasertchoung, T. Zhao, L. Chen, J. Melngailis, O. Auciello & R. Ramesh, Dynamics of ferroelastic domains in ferroelectric thin films, *Nature Mat.* 2, 43-47 (2003).

69 K. Lee and S. Baik, Ferroelastic domain structure and switching in epitaxial ferroelectric thin films, *Annu. Rev. Mat. Res.* 36, 81-116 (2006).

70 F. Xu, S. Troiler-McKinstry, W. Ren, B. Xu, Z.-L. Xie, and K.J. Hemker, Domain wall motion and its contribution to the dielectric and piezoelectric properties of lead zirconate titanate films, *J. Appl. Phys.* 89, 1336 (2001).

71 A.G. Zembilgotov, N.A. Pertsev, U. Böttger, and R. Waser, Effect of anisotropic in-plane strains on phase states and dielectric properties of epitaxial ferroelectric thin films, *Appl. Phys. Letters* 86, 052903 (2005).

72 J.X. Zhang, Y.L. Li, S. Choldhury, L.Q. Chen, Y.H. Chu, F. Zavaliche, M.P. Cruz, R. Ramesh, and Q.X. Jia, Computer simulation of ferroelectric domain structures in epitaxial BiFeO₃ thin films, *J. Appl. Phys.* 103, 094111 (2008).

73 J.J. Wang, X.Q. Ma, Q. Li, J. Briston, L.-Q. Chen, Phase transitions and domain structures of ferroelectric nanoparticles: Phase field model incorporating strong elastic and dielectric inhomogeneity, *Acta Mat.* 61, 7591-7603 (2013).

74 R. Oja, K. Johnson, J. Frantti, R.M. Niemen, Computational study of (111) epitaxially strained ferroelectric perovskites BaTiO₃ and PbTiO₃, *Phys. Rev. B* 78, 094102 (2008).

75 T. Nishimatsu, U.V. Waghmare, Y. Kawazoe, and D. Vanderbilt, Fast molecular-dynamics simulation for ferroelectric thin-film capacitors using a first-principles effective Hamiltonian, *Phys. Rev. B* 78, 104104 (2008).

76 N.A. Pertsev, A.K. Tagantsev, and N. Setter, Phase transitions and strain-induced ferroelectricity in SrTiO₃, *Phys. Rev. B* 61, R825(R) (2000).

77 Y.L. Li, S. Choudhury, J.H. Haeni, M.D. Biegalski, A. Vasudevarao, A. Sharan, H.Z. Ma, J. Levy, V. Gopalan, S. Troiler-McKinstry, D.G. Schlom, Q.X. Jia, and L.-Q. Chen, Phase transitions and domain structures in strained pseudocubic (100) SrTiO₃ thin films, *Phys. Rev. B* 73, 184112 (2006).

78 D.D. Fong, A.M. Kolpak, J.A. Eastman, S.K. Streiffer, P.H. Fuoss, G.B. Stephenson, C. Thompson, D.M. Kim, K.J. Choi, C.B. Eom, I. Grinberg, A.M. Rappe, Stabilization of monodomain polarization in ultrathin PbTiO₃ films, *Phys. Rev. Lett.* 96, 127601 (2006).

79 R.V. Wang, D.D. Fong, F. Jiang, M.J. Highland, P.H. Fuoss, C. Tompson, A.M. Kolpak, J.A. Eastman, S.K. Streiffer, A.M. Rappe, G.B. Stephenson, Reversible chemical switching of a ferroelectric film, *Phys. Rev. Lett.* 102, 047601 (2009).

80 G.B. Stephenson, M.J. Highland, Equilibrium and stability of polarization in ultrathin ferroelectric films with ionic surface compensation, *Phys. Rev. B* 84, 064107 (2011).

81 M.J. Highland, T.T. Fister, D.D. Fong, P.H. Fuoss, C. Thompson, J.A. Eastman, S.K. Streiffer, G.B. Stephenson, Equilibrium polarization of ultrathin PbTiO₃ with surface compensation controlled by oxygen partial pressure, *Phys. Rev. Lett.* 107, 187602 (2011).

82 S.M. Yang, A.N. Morozovska, R. Kumar, E.A. Eliseev, Y. Cao, L. Mazet, N. Balke, S. Jesse, R. Vasudevan, C. Dubourdieu, and S.V. Kalinin, Mixed Electrochemicalferroelectric States in Nanoscale Ferroelectrics, *Nature Physics* volume 13, pages 812–818 (2017).

83 A.N. Morozovska, E.A. Eliseev, N.V. Morozovsky, and S.V. Kalinin. Ferroionic states in ferroelectric thin films, *Phys. Rev. B* 95, 195413 (2017).

84 E.A. Eliseev, S.V. Kalinin, A.N. Morozovska, Finite size effects in ferroelectric-semiconductor thin films under open-circuit electric boundary conditions, *J. Appl. Phys.* 117, 034102 (2015).

85 A.M. Bratkovsky, A.P. Levanyuk, Continuous theory of ferroelectric states in ultrathin films with real electrodes, *J. Comput. Theor. Nanosci.* 6, 465 (2009).

86 A.M. Bratkovsky, A.P. Levanyuk, "Effects of anisotropic elasticity in the problem of domain formation and stability of monodomain state in ferroelectric films, *Phys. Rev. B* 84, 045401 (2011).

87 E.V. Chensky, V.V. Tarasenko, Theory of phase transitions to inhomogeneous states in finite ferroelectrics in an external electric field, *Sov. Phys. JETP* 56, 618 (1982) [Zh. Eksp. Teor. Fiz. 83, 1089 (1982)].

88 C.-L. Jia, K.W. Urban, M. Alexe, D. Hesse, I. Vrejoiu, Direct observation of continuous electric dipole rotation in flux-closure domains in ferroelectric Pb(Zr,Ti)O₃, *Science* 331, 1420 (2011).

89 Y.L. Tang, Y.L. Zhu, X.L. Ma, A.Y. Borisevich, A.N. Morozovska, E.A. Eliseev, W.Y. Wang, Y.J. Wang, Y.B. Xu, Z.D. Zhang, S.J. Pennycook, Observation of a periodic array of flux-closure quadrants in strained ferroelectric PbTiO₃ films, *Science* 348 547 (2015).

90 B.M. Darinskii, A.P. Lazarev, A.S. Sidorkin, Domain-wall structure near the surface of a ferroelectric, *Fiz. Tverd. Tela* 31, 287 (1989) [Sov. Phys. Solid State, 31, 2003 (1989)].

91 E.A. Eliseev, A.N. Morozovska, S.V. Kalinin, Y.L. Li, J. Shen, M.D. Glinchuk, L.Q. Chen, V. Gopalan, Surface effect on domain wall width in ferroelectrics, *J. Appl. Phys.* 106, 084102 (2009).

92 V.Ya Shur, A.L. Gruverman, V.P. Kuminov, N.A. Tonkachyova, Dynamics of plane domain-walls in lead germanite and gadolinium molybdate, *Ferroelectrics* 111, 197 (1990).

93 E.A. Eliseev, A.N. Morozovska, G.S. Svechnikov, E.L. Rumyantsev, E.I. Shishkin, V.Y. Shur, S.V. Kalinin, Screening and retardation effects on 180-domain wall motion in ferroelectrics: wall velocity and nonlinear dynamics due to polarization-screening charge interaction, *Phys. Rev. B* 78, 245409 (2008).

94 S.K. Streiffer, J.A. Eastman, D.D. Fong, C. Thompson, A. Munkholm, M.V. Ramana Murty, O. Auciello, G.R. Bai, G.B. Stephenson, Observation of Nanoscale 180 stripe domains in ferroelectric PbTiO₃ thin films, *Phys. Rev. Lett.* 89, 067601 (2002).

95 D.D. Fong, G.B. Stephenson, S.K. Streiffer, J.A. Eastman, O. Auciello, P.H. Fuoss, C. Thompson, Ferroelectricity in ultrathin perovskite films, *Science* 304, 1650 (2004).

96 V.M. Fridkin, *Ferroelectrics Semiconductors*, Consultant Bureau, New-York and London, 1980, p.119.

97 I.S. Vorotiahin, E.A. Eliseev, Q. Li, S.V. Kalinin, Y.A. Genenko, A.N. Morozovska, Tuning the polar states of ferroelectric films via surface charges and flexoelectricity, *Acta Mat.* 137, 85-92 (2017).

98 J. Bardeen, Surface States and Rectification at a Metal-Semiconductor Contact, *Phys. Rev.* 71, 717 (1947).

99 E.A. Eliseev, A.V. Semchenko, Y.M. Fomichov, M.D. Glinchuk, V.V. Sidsky, V.V. Kolos, Yu.M. Peskachevsky, M.V. Silibin, N.V. Morozovsky, and A.N. Morozovska, Surface and finite size effects impact on the phase diagrams, polar, and dielectric properties of (Sr,Bi)Ta2O9 ferroelectric nanoparticles, *J. Appl. Phys.* 119, 204104 (2006).

100 M. Y. Gureev, A. K. Tagantsev, and N. Setter *Phys. Rev. B* 83, 184104 (2011).

101 E.A. Eliseev, A.N. Morozovska, G.S. Svechnikov, Peter Maksymovych, S.V. Kalinin. Domain wall conduction in multiaxial ferroelectrics: impact of the wall tilt, curvature, flexoelectric coupling, electrostriction, proximity and finite size effects. *Phys. Rev.B.* 85, 045312 (2012)

102 Eugene A. Eliseev, Anna N. Morozovska, Christopher T. Nelson, and Sergei V. Kalinin. Intrinsic structural instabilities of domain walls driven by gradient couplings: meandering anferrodistortive-ferroelectric domain walls in BiFeO3. *Phys. Rev.B*, 99, 014112 (2019)

103 M. J. Han, E. A. Eliseev, A. N. Morozovska, Y. L. Zhu, Y. L. Tang, Y. J. Wang, X. W. Guo, X. L. Ma. Mapping gradient-driven morphological phase transition at the conductive domain walls of strained multiferroic films. *Phys. Rev. B*, 100, 104109 (2019)

104 Eugene A. Eliseev, Ivan. S. Vorotiahin, Yevhen M. Fomichov, Maya D. Glinchuk, Sergei V. Kalinin, Yuri A. Genenko, and Anna N. Morozovska. Defect driven flexo-chemical coupling in thin ferroelectric films. *Physical Review B*, 97, 024102 (2018)

105 A.K. Tagantsev, G. Gerra, and N. Setter, Short-range and long-range contributions to the size effect in metal-ferroelectric-metal heterostructures, *PRB* 77, 174111 (2008).

106 A.K. Tagantsev, L.E. Cross, J. Fousek, *Domains in Ferroic Crystals and Thin Films*, Springer, New York, 2010.

107 M.J. Haun, Z.Q. Zhuang, E. Furman, S.J. Zhang & L.E. Cross, Thermodynamic theory of lead zirconate-titanate solid solution system, part III: Curie constant and sixth-order polarization interaction dielectric stiffness coefficient, *Ferroelectrics* 99, 45-54 (1989).

108 D. Schrade, R. Müller, B.X. Xu, D. Gross, Domain evolution in ferroelectric materials: A continuum phase field model and finite element implementation, *Comput. Methods Appl. Mech. Engrg.* 196, 4365–4374 (2007).

109 B. Völker, C.M. Landis and M. Kamlah, Multiscale modeling for ferroelectric materials: identification of the phase-field model's free energy for PZT from atomistic simulations, *Smart Mater. Struct.* 21, 035025 (2012)

110 M.V. Strikha, A.I. Kurchak, and A.N. Morozovska, Integer Quantum Hall Effect in Graphene Channel with p-n Junction at Domain Wall in Ferroelectric Substrate, *J. Appl. Phys.* 125, 082525 (2019).

111 C. Ederer, and N.A. Spaldin, Effect of epitaxial strain on the spontaneous polarization of thin film ferroelectrics, *Phys. Rev. Lett.* 95, 257601 (2005).

112 N. A. Pertsev, V. G. Kukhar, H. Kohlstedt, R. Waser, Phase diagrams and physical properties of single-domain epitaxial Pb(Zr_{1-x}Ti_x)O₃ thin films, *Phys. Rev. B* 67, 054107 (2003).